

ACCEPTED MANUSCRIPT • OPEN ACCESS

Constructing High-Performance and Versatile Liquid-Solid Triboelectric Nanogenerator with Inflatable Columnar Units

To cite this article before publication: Lin Luo *et al* 2024 *Int. J. Extrem. Manuf.* in press <https://doi.org/10.1088/2631-7990/ad88bd>

Manuscript version: Accepted Manuscript

Accepted Manuscript is “the version of the article accepted for publication including all changes made as a result of the peer review process, and which may also include the addition to the article by IOP Publishing of a header, an article ID, a cover sheet and/or an ‘Accepted Manuscript’ watermark, but excluding any other editing, typesetting or other changes made by IOP Publishing and/or its licensors”

This Accepted Manuscript is © 2024 The Author(s). Published by IOP Publishing Ltd on behalf of the Institute of Machinery Manufacturing Technology.



As the Version of Record of this article is going to be / has been published on a gold open access basis under a CC BY 4.0 licence, this Accepted Manuscript is available for reuse under a CC BY 4.0 licence immediately.

Everyone is permitted to use all or part of the original content in this article, provided that they adhere to all the terms of the licence <https://creativecommons.org/licenses/by/4.0>

Although reasonable endeavours have been taken to obtain all necessary permissions from third parties to include their copyrighted content within this article, their full citation and copyright line may not be present in this Accepted Manuscript version. Before using any content from this article, please refer to the Version of Record on IOPscience once published for full citation and copyright details, as permissions may be required. All third party content is fully copyright protected and is not published on a gold open access basis under a CC BY licence, unless that is specifically stated in the figure caption in the Version of Record.

View the [article online](#) for updates and enhancements.

**Constructing High-Performance and Versatile Liquid-Solid
Trieoelectric Nanogenerator with Inflatable Columnar Units**

| | |
|------------------|--|
| Journal: | <i>International Journal of Extreme Manufacturing</i> |
| Manuscript ID | IJEM-111772.R1 |
| Manuscript Type: | Paper |
| Keywords: | solid-liquid triboelectrification, inflatable columnar structure, combined AC/DC TENG, energy harvesting, self-powered sensing |
| | |

SCHOLARONE™
Manuscripts

Accepted Manuscript

Constructing High-Performance and Versatile Liquid-Solid Triboelectric Nanogenerator with Inflatable Columnar Units

Lin Luo^{1,2}, Chao Liu^{1,2}, Rui Gu^{2,4}, Mingxia Chen^{2,3}, Yifei Wang^{2,4}, Nuo Xu^{1,2}, Yao Xiong^{2,4}, Jiahong Yang^{2,4}, Ziwei Huo^{2,4}, Yang Liu^{2,4}, Liang Wei^{1,2}, Zhong Lin Wang^{2,5,*}, Qijun Sun^{1,2,4,5,6,*}

¹Center on Nanoenergy Research, Institute of Science and Technology for Carbon Peak & Neutrality; Key Laboratory of Blue Energy and Systems Integration (Guangxi University), Education Department of Guangxi Zhuang Autonomous Region; School of Physical Science & Technology, Guangxi University, Nanning 530004, China

²Beijing Institute of Nanoenergy and Nanosystems, Chinese Academy of Sciences, Beijing, 101400, China

³Center on Nanoenergy Research, School of Chemistry and Chemical Engineering, Guangxi University, Nanning 530004, PR China

⁴School of Nanoscience and Technology, University of Chinese Academy of Sciences, Beijing, 100049, China

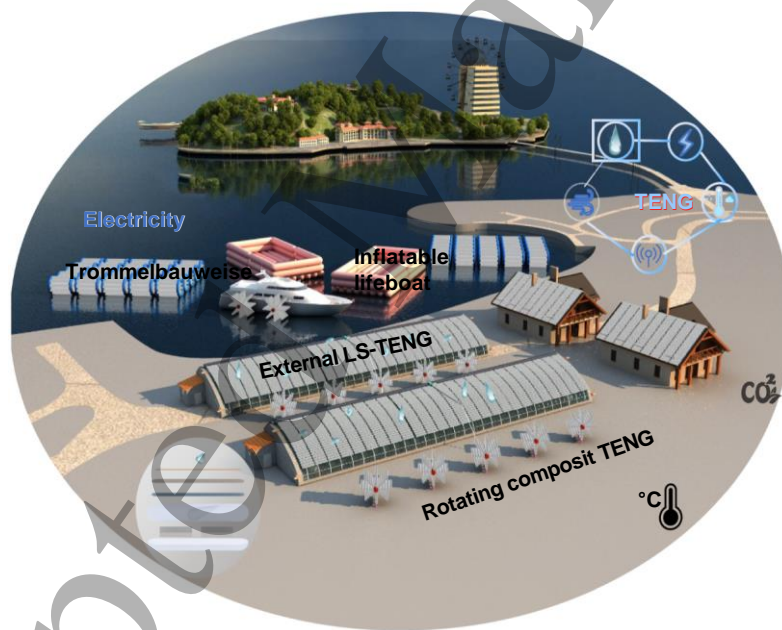
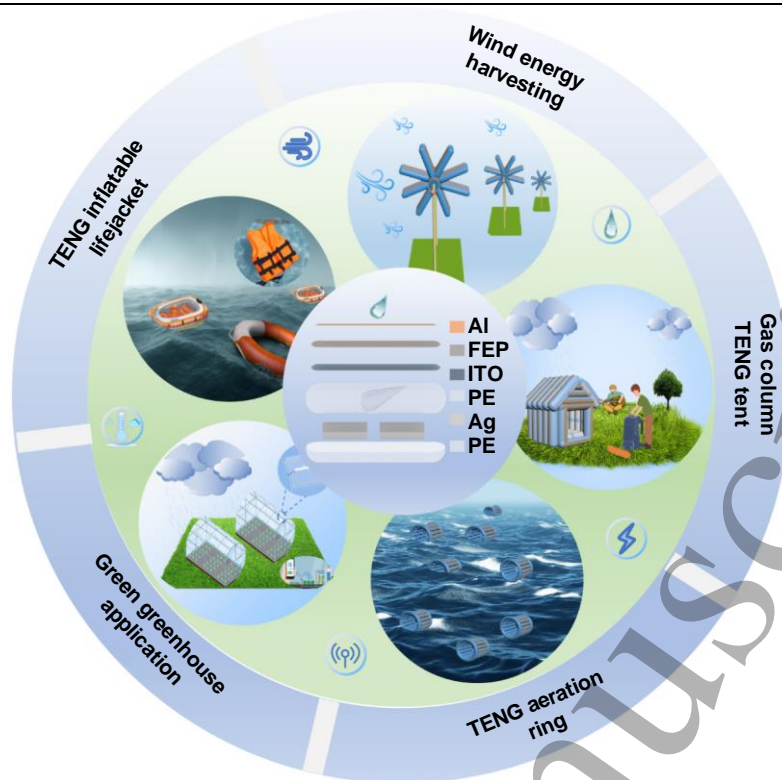
⁵Georgia Institute of Technology, Atlanta, GA, 30332, USA

⁶Shandong Zhongke Naneng Energy Technology Co., Ltd., Dongying, 257061, China

E-mail: sunqijun@binn.cas.cn, zhong.wang@mse.gatech.edu

Highlights

- In this paper, a novel and ingenious basic unit structure of aerated column is proposed.
- The AC-DC combination LS-TENG significantly improves the output performance and energy conversion efficiency.
- The LS-TENG has a multifunctional structure design that can collect energy from multiple sources simultaneously.
- LS-TENG can be used as a convenient energy source for outdoor exploration and sea rescue.
- This project can realize the wetland ecological self-powered and self-irrigation monitoring system.



Abstract

The use of water resources for energy generation has become increasingly prevalent, encompassing the conversion of kinetic energy from streams, tides, and waves into renewable electrical power. Water energy sources offer numerous benefits, including widespread availability, stability, and the absence of carbon dioxide

1
2
3 and other greenhouse gas emissions, making them a clean and environmentally friendly form of energy. In
4 this work, we develop a droplet-based liquid-solid triboelectric nanogenerator (LS-TENG) using
5 sophisticatedly designed inflatable columnar structures with inner and outer dual-electrodes. This device can
6 be utilized to harvest both the internal droplet-rolling mechanical energy and the external droplet-falling
7 mechanical energy, capable of being assembled into various structures for versatile applications. The design
8 incorporates a combined structure of both internal and external TENG to optimize output performance via
9 multiple energy harvesting strategies. The internal structure features a dual-electrode columnar-shaped LS-
10 TENG, designed to harvest fluid kinetic energy from water droplets flowing. By leveraging the back-and-forth
11 motion of a small amount of water within the air column, mechanical energy can be collected, achieving a
12 maximum mass power density of $9.02 \text{ W} \cdot \text{Kg}^{-1}$ and an energy conversion efficiency of 10.358%. The external
13 component is a droplet-based LS-TENG, which utilizes a double-layer capacitor switch effect elucidated with
14 an equivalent circuit model. Remarkably, without the need for pre-charging, a single droplet can generate over
15 140 V of high voltage, achieving a maximum power density of $7.35 \text{ W} \cdot \text{m}^{-2}$ and an energy conversion efficiency
16 of 22.058%. The combined LS-TENG with a sophisticated inflatable columnar structure can simultaneously
17 collect multiple types of energy with high efficacy, exhibiting great significance in potential applications such
18 as TENG aeration rings, inflatable lifejacket, wind energy harvesting, gas-column TENG tents, and green
19 houses.

20
21
22
23
24
25
26
27
28
29
30
31
32
33
34
35
36
37
38
39
40
41
42
43
44
45
46
47
48
49
50
51
52
53
54
55
56
57
58
59
60
Keywords: solid-liquid triboelectrification, inflatable columnar structure, combined AC/DC TENG, energy
harvesting, self-powered sensing

1. Introduction

Solid-liquid triboelectric nanogenerators (TENGs) are diminutive power-generating devices that harness electrical energy through the friction between liquid and solid surfaces [1-5]. These devices can readily convert natural energies such as raindrop and water flow into electricity [6-7], distinguished by their compact size, flexibility, and high efficiency. Typically, solid-liquid TENGs consist of multi-layered substrate with rubber (or polymer) films/conductive electrodes structures to contact with liquid mediums [8-9]. In recent years, solid-liquid TENGs have emerged and found applications in a variety of circumstances, including low-speed water flows [10], raindrops, liquid-interface [11], and biological surface friction, thereby offering power and energy harvesting capabilities [12-14]. Given their environmentally friendly and renewable nature, TENGs

1
2
3 hold significant potential for application in all-optical liquid flow sensor [12-13], wearable devices, and
4
5 medical instruments [14].

6
7 Research in solid-liquid energy harvesting technology can be traced back several decades when scientists
8
9 began studying the triboelectrification effect between surface micro/nano-structured materials [15-16]. They
10
11 discovered that minuscule charge transfer occurred at the microscopic level when solids and liquids came into
12
13 contact [16-18]. With the invention of TENG by Z L Wang's team in 2012 [19], the study of solid-liquid-
14
15 contact induced charge transfer has also begun to attract widespread attention. Lin and Chen designed a TENG
16
17 based on the contact between polydimethylsiloxane (PDMS) with a pyramid surface and water. Its
18
19 instantaneous power approached $0.13 \text{ W}\cdot\text{m}^{-2}$, thus showcasing the potential for liquid-driven TENG [20].
20
21 Soon after, Choi and Lee invented the first TENG that collected kinetic energy from flowing water through
22
23 contact electrification in a tubular system, enhancing the applicability of water-driven TENG [21]. In order to
24
25 explore the application of solid-liquid TENG to detect different flow rates, Chen and Guo utilized liquid
26
27 droplets passing through capillaries to study single-electrode microfluidic sensors, indicating significant
28
29 potential for self-powered trace analysis [22]. As opposed to energy sources such as liquid drops and water
30
31 flow, Earth's ocean coverage extends up to 70%. Accordingly, Z L Wang's group proposed a completely
32
33 different method for scavenging the ocean's wave power in floating nets in 2017. Consequently, the
34
35 development of TENG networks to harness renewable energy from the sea has instigated a wide range of
36
37 research and utilization [23]. By employing a new circuit model, a high-power droplet-based TENG was
38
39 developed by Z L Wang's group in 2020 with a single-device achieving an instantaneous power density of up
40
41 to $50.1 \text{ W}\cdot\text{m}^{-2}$ [24]. On the other hand, by utilizing the high-voltage output properties of the TENG, a
42
43 triboelectric contactless charge injection method has been proposed to enable continuous corona discharges
44
45 and manipulation of large-volume droplets [25]. Alternating/direct current convertible outputs can also be
46
47 readily achieved by synergistically utilizing electrostatic induction/discharge and triboelectrification effects
48
49 [29]. Although essential technical breakthroughs and key research achievements concerning solid-liquid
50
51 TENG have been accomplished, energy conversion efficiency, multifunctionality, and stability are still
52
53 inadequate [26-28]. Further enhancement is necessary, especially to meet larger-scale energy demands in
54
55 practical applications. It is imperative that a synergistic approach integrating theoretical research and
56
57 engineering practice be pursued, on the basis of continued study and innovation in the field of solid-liquid
58
59 triboelectrification [29-30]. For instance, Zi Group designed a water-tube-based TENG that achieved an

1
2
3 ultrahigh volume density of $9 \text{ mC}\cdot\text{m}^{-3}$ output, capable of collecting multiple types of energy [31]. Drawing
4 inspiration from their sophisticated design, more column-/tube-structured solid-liquid TENGs with high
5 conversion efficiency are also available to be manufactured. The inflatable column unit is one of the excellent
6 candidates, which can not only provide enough space for the inner liquid but also form a proper contact arc
7 angle for external waterdrops. It is also lightweight, facile to manufacture, mass-productive, and cost-effective,
8 which can be directly utilized as the crucial friction material and provide diverse options and configurations.
9
10
11
12
13

14
15 In this work, we have developed a liquid-solid TENG (LS-TENG) with a combined output of both
16 alternating current (AC) and direct current (DC) [32-33]. The basic structure of this device employs an
17 elaborately designed inflatable column model with both internal and external electrodes. This device is able
18 to collect mechanical energy from the rolling of internal liquid droplets as well as from the falling of external
19 liquid droplets, and the combined AC/DC output significantly enhances its performance. The novel and
20 versatile design of this device allows it to be used for converting and collecting energy from various sources,
21 such as wind, rain, mechanical motion, and ocean waves. Its applications can span across multiple fields,
22 including but not limited to greenhouses, wind turbines, tents, inflatable cylinders, and lifeboats. Its
23 capabilities can provide self-powered monitoring for wetland ecological projects and enable rescue operations
24 at sea. Additionally, the external LS-TENG has the potential for raindrop sensing and can be applied in the
25 monitoring of rainfall and rain velocity.
26
27
28
29
30
31
32
33
34
35
36

37 This study explores the output performance and charging behavior of the LS-TENG through rigorous
38 simulations and practical applications. The optimal position for the droplet angle, falling height, and effective
39 contact area of the external LS-TENG are meticulously investigated. Furthermore, the study discusses the
40 mechanism of generating AC and DC power through liquid-solid contact and analyzes the high output
41 principle from a circuit model perspective. This study also determines the optimal volume ratio of the injected
42 water and the inflatable column membrane in the inner LS-TENG, as well as the influence of rotational
43 frequency. A comprehensive comparison of the cumulative charging speeds of the external, inner, and
44 combined TENG demonstrates the significant enhancement of the output performance through the stacking
45 effect of the combined LS-TENG. Compared to conventional LS-TENGs, the combined LS-TENG can
46 simultaneously collect multiple types of energy and has a more diverse range of applications [34-35]. Its
47 lightweight and convenient structure not only allows for energy harvesting but also provides wind protection,
48 warmth, and increased buoyancy. The integrated design is versatile, enabling self-powering rain gauge and
49
50
51
52
53
54
55
56
57
58
59
60

rain velocity sensing in addition to energy harvesting.

2. Results and Discussion

2.1 Structural design and application scenarios

Figure 1(a) illustrates the front structural and perspective drawing of one single LS-TENG unit. Within the frame, liquid water oscillates within the inflatable columnar unit, facilitating electron transfer through contact-electrification with the plastic column-wall [36]. The structure incorporates two segments of silver fabrics serving as inner electrodes, generating AC electrical signals as the water moves back and forth. A layer of water-resistant plastic film is located beneath these electrodes. The upper section of the inflatable column unit is tailored for raindrop energy harvesting, employing indium tin oxide (ITO) and aluminum (Al) as electrodes and fluorinated ethylene propylene (FEP) as the triboelectric layer, with the air column acting as the structural backbone. DC signals can be generated when raindrops come into contact with the FEP (leading to triboelectrification with the Al electrode and subsequently through the ITO electrode). **Figure 1(b)** depicts a holistic scenario and the vision of the combined LS-TENG's versatile applications; **Figure 1(c)** exemplifies the versatility of the fundamental design for energy harvesting, which can be adapted for water rollers, inflatable lifeboats/lifejackets, specifically designed for ocean and rainwater energy harvesting. Furthermore, it can be manufactured in windmill structures for simultaneously harvesting mechanical energy from wind and rainfall; it can also be fabricated as inflatable-structured building blocks for portable tents to harvest kinetic energy during motion; it is also available to construct agricultural greenhouses by employing transparent inflatable columns, which can facilitate extensive raindrop energy harvesting, self-powering the sensors to monitor rainfall and temperature-humidity conditions, along with enhanced protection against wind and greenhouse warming. Photographs of related device architectures for diverse applications are presented in **Figure 1(d)** (corresponding manufacture process is shown in **Figure S1**). Along with such broad applications, output stability is primary for the LS-TENG and first evaluated as shown in **Figure 1(e)**. Both the internal open-circuit voltage (V_{OC}) and external DC signal within a single unit device are evaluated to be stable over 6 000 s. The analysis reveals that the internal V_{OC} is stable at ~ 91 V, while the external DC signal fluctuates around (128.5 ± 6.5) V. Detailed electrical output signals can be found in **Figure S2(a)** and **(b)**. Notably, the liquid water encapsulated in the inflatable columnar unit can be restored for over 40 days (**Figure S2(c)**) without mass loss due to the excellent sealing process in this work. Besides, the liquid water is selected

1
2
3 as the friction material for the inner TENG instead of commonly utilized polytetrafluoroethylene (PTFE)
4 spheres, which is demonstrated to produce higher output performances (**Figure S3**).

5 6 7 8 9 2.2 Working mechanism and device design

10
11 LS-TENGs can convert mechanical energy, generated from the contact between liquid and solid interfaces,
12 into electrical energy [37-38]. Their operational principle is rooted in electrostatic induction effect and charge
13 separation phenomenon induced by contact-electrification between solids and liquids [39]. This occurs due to
14 the redistribution of surface charges caused by friction, which leads to a certain quantity of positive charges
15 on the solid surface and negative charges on the liquid surface [40]. Consequently, a potential difference
16 between the liquid and solid materials is created and induces the output electrical energy from the LS-TENG
17 (fundamentally relying on the potential difference and charge transfer process) [41].

18
19
20
21
22
23
24
25 In this work, the combined LS-TENG is capable of generating both AC and DC signals [42]. **Figure 2(a)**
26
27
28
29
30
31
32
33
34
35
36
37
38
39
40
41
42
43
44
45
46
47
48
49
50
51
52
53
54
55
56
57
58
59
60
of an AC [46].

1
2
3 The external LS-TENG generates electrical signals via the contact-electrification interaction between
4 falling droplets and the coated FEP on the external column surface. It incorporates the FEP film covered on
5 an ITO electrode, with another Al electrode positioned on one side of the FEP film and connected to an
6 external load to establish the circuit. When the polar water droplet falls on the non-polar FEP film, electrostatic
7 effects are induced due to charge transfer between the two materials [47]. The primary mechanisms driving
8 charge transfer and electrostatic induction effects for the external LS-TENG are electron hopping and charge
9 transfer [48]. During the friction process, molecules on the FEP surface will be squeezed and pulled by water
10 molecules, potentially concentrating electrons in the stressed area and causing electron hopping as shown in
11 **Figure 2(b)**. As a result, a portion of the electrons transfers from water molecules to the FEP surface.
12 Simultaneously, given that FEP has low electron affinity, it may weakly attract and transfer electrons during
13 the friction process, leading to the formation of local positive charges within the water molecules. The process
14 of electron hopping and transfer results in an uneven distribution of charges, which subsequently leads to the
15 formation of charged FEP and water molecules and generates an electrostatic field. Under the influence of this
16 electrostatic field, molecules possessing identical charges repel each other, while those with differing charges
17 attract one another. This attraction and repulsion result in charge transfer and the manifestation of electrostatic
18 induction effects [49]. The external LS-TENG generates DC output, which can be attributed to the separation
19 and accumulation of charges induced by the unidirectional friction process [50].

20
21
22
23
24
25
26
27
28
29
30
31
32
33
34
35
36
37 **Figure 2(c)** delineates the operational mechanism of the combined LS-TENG. The principle underpinning
38 the internal LS-TENG is described as follows. **Figure 2(c-i)** presents the electrical characteristics of the
39 droplet in its initial position. As the droplet slides from the left electrode to the central region, an electrostatic
40 induction effect prompts electrons to traverse from the left electrode to the right electrode via the external
41 circuit (**Figure 2(c-ii)**) [51]. Upon reaching a point where the droplet reaches the overlapping position against
42 the right electrode (**Figure 2(c-iii)**), all electrons will flow towards the right electrode. Subsequently, as the
43 droplet slides backward (**Figure 2(c-iv)**), electrons will transfer from the right electrode to the left electrode
44 via the external circuit, thereby generating a reverse current [51]. In the context of the external LS-TENG,
45 upon making contact with the FEP surface, the droplet begins to spread around the impact point on the FEP.
46 This process gradually increases the contact area between the solid and liquid interfaces. Once this contact
47 area reaches its maximum value, the droplet begins to shrink and the contact area decreases (the physical shape
48 of the droplet continuously changes). Ultimately, due to surface tension, these dispersed droplets coalesce,

1
2
3 flow over, and exit from the FEP surface, as shown in **Video S1**. Notably, when the droplet fully contacts the
4 solid surface and completes triboelectric charging at the interface, the shape of the droplet begins to shrink
5 slowly, which means the separation process of the solid-liquid interface is continuous rather than instantaneous.
6
7 Therefore, charge transfer based on traditional electrostatic induction is also non-instantaneous, resulting in
8
9 discrete and weak electrical signals over a period [52].
10
11

12
13 From a circuit perspective, under the impact of the droplet, FEP can serve as an ideal charge storage
14 medium with an equal amount of opposite charges induced on ITO, thereby facilitating potential charge
15 transfer to the Al electrode [53]. When the falling droplet spreads on the FEP surface, it bridges the initially
16 disconnected components (FEP/ITO and Al electrode) into a closed-loop electrical system and instantaneously
17 conducts. The circuit analysis, as shown in **Figure S4**, establishes a capacitor pair (C_P) with water/FEP serving
18 as the top plate and FEP/ITO as the bottom plate. An additional capacitor, C_1 , is present at the water/FEP
19 interface. Prior to the droplet's contact with the aluminum electrode, no capacitor forms at the water/Al
20 interface, leading to the C_P and C_1 remaining open-circuited with no charge flow between them. Conversely,
21 when the Al electrode and FEP are connected via the liquid (in conduction mode), another capacitor, C_2 , forms
22 at the water/Al interface, thereby creating a closed circuit as shown in **Figure S4(b)**.
23
24
25
26
27
28
29
30
31
32

33 Upon further examination of the mechanism depicted in **Figure 2(c)**, it becomes evident that after a
34 droplet falls from a height and makes contact with FEP, this process will make the droplet carry a positive
35 charge, while FEP carries a negative charge. As the droplet shrinks, the unneutralized negative charges on the
36 surface of FEP gradually increase. To maintain electrostatic equilibrium, equal amounts of positive charges
37 are induced on the conducting layer. This process triggers the migration of free electrons through the external
38 circuit [52]. Notably, this process is not instantaneous; rather, it occurs gradually as the charges are
39 continuously induced and transferred until reaching the minimal current level. Upon making contact with the
40 Al electrode, the droplet immediately conducts, initiating a cycle where the accumulated positive charge is
41 instantly released, resulting in pronounced current and voltage peaks. **Figure 2(d)** illustrates the potential
42 distribution of internal droplet at four distinct positions, as confirmed by finite element analysis (COMSOL
43 Multiphysics). This analysis also simulates the potential distribution throughout the process of droplet sliding.
44
45
46
47
48
49
50
51
52
53
54
55
56
57
58
59
60

Figure S5 presents a detailed finite element analysis on the potential distribution for both the external LS-TENG and the overall combined LS-TENG.

2.3 Characterization of the output performance of inner TENG

In order to achieve high output performance from the designed LS-TENG, we have manufactured five internal LS-TENG units and integrated them in series, as shown in **Figure 3(a)**, and photo images in **Figure 3(b)**. **Figure 3(c)** further provides a rudimentary schematic representation of the triboelectrification process for a single LS-TENG unit to understand the detailed process of charge transfer during the inner droplets oscillate/flow back and forth. To extract the operational conditions for the optimal output, we have studied the factors influencing the output of the internal LS-TENG. **Figure 3(d)-(f)** present a comparative analysis of V_{OC} , short-circuit current (I_{SC}), and transferred charges (Q_{SC}) across varying frequencies while maintaining a consistent variable (e.g., air column volume and water injection volume). The output performance initially escalates with increasing frequency, peaking at an optimal output performance at a frequency of 1.75 Hz ($n = \omega/2\pi = 1/T = f$, where n is the rotational speed, ω is the angular velocity, and f is the frequency) [54], achieving maximum output values of $V_{OC} = 84.134$ V, $I_{SC} = 0.495$ μ A, and $Q_{SC} = 30.266$ nC. The output then gradually decreases as the frequency further increases to 2 Hz. This phenomenon can be explained as follows: the initial increment in operation frequency increases the effective contact area between the droplet and the inflatable column wall; however, further increased frequency leads to insufficient contact between the droplet and the column wall, resulting in an optimal working frequency at 1.75 Hz. Additionally, **Figure S6** provides the frequency-related output characteristics based on the series connected inner LS-TENGs.

Figure 3(g)-(i) delineate the correlation between various water injection volumes (2, 4, 8, 16, and 24 ml) and output performance at 1.5 Hz, suggesting an optimal water injection volume of 16 ml. This phenomenon can be explained from that larger droplet volume results in bigger contact area but a simultaneously decreased movement distance, which will result in an optimal volume for the water droplet. Upon examining of individual unit, it can be deduced that the maximum output is achieved when the volume ratio between water and column structure (C_{H_2O}/C_{column}) approximates to $1/9\pi$. When examining individual units, it is observed that the maximum output can be achieved when the volume ratio between water and column structure (C_{H_2O}/C_{column}) approaches $1/9\pi$ (detailed characterizations in **Figure S7**).

To demonstrate a potential application scenario, **Figure 3(j)** schematically illustrates the harvesting of water wave energy using a rudimentary lifeboat constructed from the integrated inner LS-TENG units to construct. This lifeboat comprises six air columns each measuring 48π cm³ in volume, and injects approximately 5 ml of water (this is obtained according to the optimal volume ratio of $1/9\pi$) into each column

to form an air column boat. Corresponding output performances of the lifeboat driven by water waves at a frequency of 1.75 Hz are evaluated as shown in **Figure 3(k)**, indicating $V_{OC} = 228.99$ V, $I_{SC} = 2.321$ μ A, and $Q_{SC} = 163.21$ nC.

2.4 Characterization of the output performance of external TENG

Figure 4(a) shows the dynamic droplet sliding process for the external LS-TENG, in which the spreading area and detailed sliding process of the droplet before and after contact with the Al electrode can be clearly observed. To select the optimal materials for the external LS-TENG, we have characterized and compared the output performance based on different electrodes and friction materials, as shown in **Figure S8**. After characterization, we choose ITO-Al as the electrode and FEP as the friction layer, as schematically illustrated in **Figure 4(b)**. Commonly, different flow rates (or dropping speeds) of the water droplets have a direct impact on the output performance of the external LS-TENG. As shown in **Figure 4(c)**, the statistical results of output performances at varying flow rates indicate an initial increment with increasing flow rate and a subsequent decrement, reaching the peak value at 22.5 ml. **Figure 4(d)** further displays the detailed maximum outputs for the external LS-TENG contacting with one single droplet, resulting in V_{OC} of 141.62 V, Q_{SC} of 83.582 nC, and I_{SC} of 43.837 μ A.

There are also many key factors that influence the output performance of the external LS-TENG [41], including the droplet descent height (**Figure 4(e)**) and inclination angle (**Figure 4(h)**). Corresponding output performances at different descent heights (5, 10, 20, and 40 cm) are characterized in **Figures 4(f)** and **(g)**, which reveal that the V_{OC} , I_{SC} , and Q_{SC} of LS-TENG progressively increase with the droplet descent height [55]. This means increasing droplet descent height results in a larger spreading area on the FEP, which thereby leads to a gradual increase in the LS-TENG output performance of V_{OC} , I_{SC} , and Q_{SC} with increasing droplet descent height. As the contact point between the droplet and the FEP directly affects the contact area, we have also verified this point by characterizing the variation in output performance at different droplet inclination angles in **Figure 4(i)** and **(j)**, revealing the optimal output performance achieved at a 45° angle. **Figure S9** illustrates the characterization of droplets contacting the FEP at different positions. The first signal represents droplets away from the Al electrode, the second signal corresponds to droplets above the Al electrode, the third signal represents droplets directly in the middle of the Al electrode, and the last signal represents droplets below the Al electrode. It is worth noting that the highest output performance can be observed when the droplet

falls directly above the Al electrode. This is because at this point, the droplet has not yet contracted, maximizing the spreading area (described in detail in **Figure S10** by plotting Q_{SC} vs. three influencing factors). The design of the circuit connection method for multiple external LS-TENG is shown in **Figure S11**.

2.5 Output power characterization and charging applications

To demonstrate the versatile applications of the LS-TENG, **Figure 5(a)** first illustrates a three-dimensional schematic of a windmill manufactured using the combined LS-TENGs [56]. The rotation of the windmill in response to wind causes the internal water to continuously roll in each LS-TENG (**Figure S12**), thereby generating electrical signals via the liquid-solid contact triboelectrification process [57]. **Figure 5(b)** shows the output performance of the inner LS-TENG of one single fan blade, which consists of 36 combined LS-TENG units. This structural design results in a maximum V_{OC} of 385.7 V, an I_{SC} of 3.668 μA at its peak, and a maximum Q_{SC} of 2.6 027 μC . This output is sufficient to illuminate 120 in-series connected LED lights as demonstrated in **Figure 5(c)**. The output voltage of the windmill increases proportionally with external resistance, reaching a peak power output of 0.676 mW when the load resistance is set at 100 M Ω (**Figure 5(d)**). **Figure 5(e)** presents the charging curves for capacitors of various capacities—33 μF , 47 μF , 100 μF , 220 μF , and 330 μF —with the 33 μF capacitor charging to 3 V in 210 s. An electronic watch can be readily powered by the rotation of the windmill driven by a rotary motor (which corresponds to the charging curve in **Figure 5(f)**). For the practical application of harvesting mechanical energy from multiple droplets energy by the external LS-TENG component, a custom facility with multiple needles driven by a digital-controlled precise motor is established as shown in **Figure 5(g)**. The charging curves for different capacitors by a single droplet are shown in **Figure 5(h)**, indicating that a 47 μF capacitor can easily reach 3 V within 130 seconds. The output voltage/power curves vs. different load resistances produced by a single droplet are displayed in **Figure 5(i)**, revealing that the output power first increases with resistance and then decreases, reaching a peak power output of 4.41 mW at 1 M Ω . The process of illuminating LEDs and powering a temperature and humidity sensor with the external LS-TENG under the influence of one single droplet is detailed in **Video S2** and **Video S3**.

2.6 Combined LS-TENG for practical applications and outlook

After investigating the individual output characteristics of the inner and external LS-TENGs, we subsequently evaluate the output performances of the combined LS-TENG. As shown in **Figure 6(a)**, schematic representation of a windmill constructed by the combined LS-TENG is demonstrated to concurrently harvest wind and rain energy. **Figure 6(b)** displays the energy conversion efficiency for both internal and external TENG, yielding a wind-to-electric energy conversion efficiency of 10.358% and a rain-to-electric energy conversion efficiency of 22.058% [58]. The corresponding equations on evaluating the energy conversion efficiency are listed as follows:

$$E_1 = mgh$$

$$E_1' = \frac{1}{2}mv^2$$

$$E_2 = \oint UdQ = \int_0^T I^2 R dt$$

$$\eta = E_1/E_2$$

in which E_1 represents the total mechanical energy of the falling raindrops for the external TENG, m represents the mass of a single droplet, and h is the falling height of the droplet. E_1' is the total mechanical energy of the inner TENG moving back and forth, and v is the speed at which the water droplets move back and forth. E_2 is the basic formula for calculating effective electrical energy. The energy conversion efficiency (η) can be calculated by using E_1/E_2 . In **Figure S13**, we have compared the energy conversion efficiency of our LS-TENG with other droplet TENGs, and it is apparent that our conversion efficiency is significantly higher than previous reports [24, 59-62].

Figure 6(c) illustrates the charging curves for a 100 μ F capacitor by inner, external, and combined LS-TENG, respectively. The combined output from both internal and external LS-TENGs significantly outperforms the individual output of each type of LS-TENG. As a proof of concept for self-powered sensation, **Figure 6(d)** further depicts a flowchart for the practical application of the combined LS-TENG in a greenhouse setting (more detailed explanations in **Figure S14**). Here, an external LS-TENG is deployed to harvest mechanical energy from raindrops and implement the real-time monitoring. Every time it rains, electrical signals are generated by raindrops falling on the external LS-TENG, which can also be utilized to activate an alarm. Factors such as raindrop speed and volume can significantly influence these electrical sensing signals. The frequency of the alarming process can be indicative of the amount of precipitation, as illustrated in **Video S4**. During long-period of rainfall, the LS-TENG can also harvest the mechanical energy and utilize the

converted electricity to power an automated irrigation system with soil humidity sensors. This system will trigger a control signal to relevant terminals when the humidity level drops below a certain threshold. Furthermore, the windmill-structured TENG can also be used for greenhouse and simultaneously harvest the kinetic energy brought by both the wind and the raindrops to supply the self-irrigation system. The corresponding circuit diagram is depicted in **Figure 6(e)**, which shows that the outputs from both types of TENGs are rectified to charge a capacitor, which then powers sensors linked to appliances (e.g., transmitting temperature and humidity data to a smartphone as shown in **Figure 6(f)**). For instance, the converted mechanical energy from raindrops can be stored and used for automatic irrigation (**Video S5**). Furthermore, **Figure 6(g)** offers a comprehensive perspective on the practical applications of the proposed LS-TENGs constructed from the inflatable columnar units. In this scenario, the wind and rain energy can be readily scavenged by either inner or external LS-TENGs constructed on the greenhouse concurrently, facilitating rain detection and autonomous environmental monitoring within the greenhouse.

3. Conclusions

In summary, a combined LS-TENG is proposed and utilized for harvesting fluid dynamic energy from water droplets. This makes it suitable for versatile applications such as rooftops, greenhouse roofs, and windmills, where it can simultaneously harvest wind and rain energy (**Figure S15**). It also exhibits extensive potential in marine energy applications (**Figures S16, S17**). A single external LS-TENG can also function as a raindrop sensor, providing real-time rainfall intensity monitoring. Its practical implementation in wetland ecological projects could potentially facilitate self-powered wetland surveillance and supply energy for marine rescue operations. Based on the simulations and practical demonstrations of the LS-TENGs, the output performances, charging behaviors, and some critical influence factors (e.g., device size, droplet's falling height, inclination angle, and contact position) are investigated in detail, which is crucial for the configuration optimization and volumetric ratio identification for the LS-TENGs. The evaluated maximum output for external LS-TENG with a single droplet is recorded at $V_{OC} = 141.82$ V and $I_{SC} = 43.837$ μ A, with an optimal inclination angle of 45° and a falling height of 1 m, achieving the peak power density of 7.35 $W \cdot m^{-2}$ [63]. The maximum output for the inner LS-TENG constructed windmill fan is evaluated with the $V_{OC} = 228.99$ V and $I_{SC} = 2.321$ μ A, with an optimal liquid column volumetric ratio of $1/9\pi$, resulting in a peak power density of 9.02 $W \cdot Kg^{-1}$ (**Figure S18**). When the combined LS-TENGs are integrated into a compact windmill design for dual-modal harvesting

of wind and rain energy, it can instantly illuminate 150 LEDs. Notably, the liquid droplet used for the LS-TENG can also be readily extended to either ionic solution or oil, broadening the applications of LS-TENGs (Figure S19). This work proposes a sophisticated design for harvesting the liquid-solid related mechanical energy by using inflatable structures, which exhibits versatile possibilities and significant potentials for the applications toward multifunctional lifejackets and lifeboats, energy-harvesting raincoats and umbrellas with warm and windproof functions, and high-efficient harvesting of water wave energy and raindrop energy.

4. Experimental Section

4.1 Materials

The experiment involved the active materials such as plastic films (PE), deionized water, conductive silver fabric, adhesive ITO (resistance of 5 Ω , thickness of 0.125 mm), FEP film (thickness of 0.08 mm), and adhesive double-sided conductive aluminum foil (thickness of 0.06 mm). All materials were procured from commercial suppliers.

4.2 Manufacture of the TENG

This paper describes a combined LS-TENG, wherein deionized water and plastic film serve as the friction layers. A certain volume of deionized water is sealed within an individual plastic film (9 cm \times 2.5 cm) and inflated to form an air column shape. Silver fabric (3.2 cm \times 2.5 cm) is used as two electrodes on the inner surface of the plastic film (spaced by 1.5 cm), with waterproof sealing applied to the silver fabric electrode area. As deionized water flows back and forth between the two electrodes, friction between the water and plastic film facilitates charge transfer, producing an alternating current signal through the electrodes, thus forming a simple independent layer mode TENG. The external design features a droplet-type LS-TENG, using the aforementioned plastic film as a substrate with stripe-structured ITO electrode. Attach the polarized FEP film to the outside of the silver fabric and connect aluminum foil of the same length with ITO (width: 3 mm) as the electrode to the FEP. When a droplet comes into contact with both the FEP and the Al electrode, the circuit is instantaneously completed, generating a direct current signal output (single droplet-device contact area of 1 \times 6 cm²). These two structures combine together to form the final combined LS-TENG.

4.3 Structural design and manufacturing process

The device can be applied for the conversion and utilization of energy from wind, rain, marine sources,

1
2
3 and kinetic energy. The design for wind and rain energy collection starts with 3D printing of the support
4 structure and the rotating shaft, as shown in **Figure S12**. Six individual composite structure TENGs are
5 grouped together to form a rotating blade, with six such groups in total. The blades are assembled onto the
6 shaft, which is designed with a hollow interior to facilitate the integration of the circuitry while also reducing
7 the weight for easier wind-driven rotation. The roller structure consists of ten LS-TENGs measuring 9 cm in
8 length and 2.5 cm in width, which are assembled in the form of rollers designed to be integrated in multiple
9 rollers in order to be spread on the water surface to harvest ocean energy. The yacht design, on the other hand,
10 consists of six LS-TENG inflatable columns with dimensions of 15 cm in length and 4 cm in width. In this
11 paper, a comprehensive characterization and performance evaluation of the combined LS-TENG of these two
12 sizes are presented. The mass of the individual components of the windmill and roller model is about 2.49 g,
13 while the mass of the individual components of the yacht model is 8,279 g.

24 4.4 Experimental setup

25
26
27 The experimental setup required to perform the experiments for the performance evaluation of LS-TENG
28 starts with the design of the LS-TENG structure, including the blade shape, material selection and assembly
29 method. This involves an in-depth understanding of the material properties and engineering design principles
30 to ensure excellent and stable performance of the LS-TENG. The laboratory environment is maintained at
31 well-controlled conditions, including temperature, humidity, and dust control, to avoid interference with
32 results from external environmental factors. A rotary motor is utilized to provide the rotational power required
33 by the LS-TENG. The rotational speed is precisely controlled and the rotational parameters in each experiment
34 are recorded. Highly accurate data acquisition equipment, such as electrometer (e.g., Keithley 6514 system),
35 is used to measure the output voltage, short-circuit current, and transferred charges of the LS-TENG under
36 different conditions. Different external load resistors are connected in series to the LS-TENG to evaluate its
37 output power performance under different load conditions. For charging experiments, the LS-TENG is
38 connected in parallel with a capacitor and Keithley 6514 (used to monitor the real-time voltage change across
39 the capacitor). When the raindrop simulation experiment is conducted, a jet pump is customized to simulate
40 the rate and pattern of raindrop falling and to ensure that the raindrops can fall uniformly on the surface of the
41 LS-TENG. During the whole experimental process, every step of operation, parameter setting in detail, and
42 the output performances of LS-TENG are recorded for subsequent data analysis. Based on the above
43 experimental setup, the LS-TENG performances are systematically evaluated for further optimization and
44
45
46
47
48
49
50
51
52
53
54
55
56
57
58
59
60

potential practical application.

4.5 Characterization and measurement

The internal LS-TENG performance of individual blades is characterized by using a rotating motor to set different speeds, and the open-circuit voltage, short-circuit current, and transferred charge under different influencing factors are measured using an electrometer (Keithley 6514 system). The output voltage under different loads is measured by a Keithley 6514 electrometer connected in parallel. Based on the output voltage, current, and power characteristics relative to the external load resistance. The peak power for the corresponding external load resistance is calculated using the formula $P = P_R$, where P , V , and R represent the peak power for the resistance load, the measured output voltage, and the resistance, respectively. The average power is calculated based on $P = \int_0^T U^2 / R dT$. When charging capacitors, a Keithley 6514 electrometer connected in parallel with the capacitor can also be used to monitor the voltage across different capacitors. External raindrop characterization is performed using an injection pump to simulate raindrop falling.

4.6 Finite element simulation

COMSOL Multiphysics software is utilized to simulate the electric potential based on the electrostatic module. The droplet radius is set at 0.5 mm, maintaining contact with the solid surface. Equal and opposite surface charge densities are set for the droplet and dielectric layer. The bottom faces of the two electrodes are grounded. Parameter scanning is conducted for the horizontal movement of the droplet to study the changes in electric potential.

Acknowledgement

This work is financially supported by the National Key Research and Development Program of China (2023YFB3208102, 2021YFB3200304), the National Natural Science Foundation of China (52073031), Beijing Nova Program (Z211100002121148), Fundamental Research Funds for the Central Universities (E0EG6801X2), and the “Hundred Talents Program” of the Chinese Academy of Sciences.

References

- [1] Liang X, Liu S J, Lin S Q, Yang H B, Jiang T and Wang Z L. 2023. Liquid–solid triboelectric

nanogenerator arrays based on dynamic electric-double-layer for harvesting water wave energy. *Adv. Energy Mater.* **13**, 2300571.

[2] Liu D, Yang P Y, Gao Y K, Liu N, Ye C Y, Zhou L L, Zhang J Y, Guo Z T, Wang J and Wang Z L. 2024. A dual-mode triboelectric nanogenerator for efficiently harvesting droplet energy. *Small* **20**, 2400698.

[3] Jung H, Ouro-Koura H, Salalila A, Salalila M and Deng Z D. 2022. Frequency-multiplied cylindrical triboelectric nanogenerator for harvesting low frequency wave energy to power ocean observation system. *Nano Energy* **99**, 107365.

[4] Cao L N Y, Su E M, Xu Z J and Wang Z L. 2023. Fully enclosed microbeads structured TENG arrays for omnidirectional wind energy harvesting with a portable galloping oscillator. *Mater. Today* **71**, 9-21.

[5] Dassanayaka D G, Alves T M, Wanasekara N D, Dharmasena I G and Ventura J. 2022. Recent progresses in wearable triboelectric nanogenerators. *Adv. Funct. Mater.* **32**, 2205438.

[6] Gonçalves I, Rodrigues C and Ventura J. 2024. Sea state adaptation enhances power output of triboelectric nanogenerators for tailored ocean wave energy harvesting. *Adv. Energy Mater.* **14**, 2302627.

[7] Wang W L, Yang D F, Yan X R, Wang L C, Hu H and Wang K. 2023. Triboelectric nanogenerators: the beginning of blue dream. *Front. Chem. Sci. Eng.* **17**, 635-678.

[8] Cui L L, Song M H, Kong Y X, Cheng L, Wang D, Xiao Y H and Jiang J. 2009. The comparative studies of charge storage stabilities among three PP/porous PTFE/PP electret. *J. Electrostat.* **67**, 412-416.

[9] Zhao D, Li H Y, Wang J L, Gao Q, Yu Y, Wen J M, Wang Z L and Cheng T H. 2023. A drawstring triboelectric nanogenerator with modular electrodes for harvesting wave energy. *Nano Res.* **16**, 10931-10937.

[10] Dai J H, Xia X, Zhang D, He S S, Wan D, Chen F M and Zi Y L. 2024. High-performance self-desalination powered by triboelectric–electromagnetic hybrid nanogenerator. *Water Res.* **252**, 121185.

[11] Fu J J, Xu G Q, Wu H, Li C Y and Zi Y L. 2022. Liquid-interfaces-based triboelectric nanogenerator: an emerging power generation method from liquid-energy nexus. *Adv. Energy Sustainability Res.* **3**, 2200051.

[12] Su L, Xiong Q, Zhu Y Y and Zi Y L. 2022. A liquid–solid contact electrification based all-optical liquid flow sensor for microfluidic analysis in biomedical applications. *Adv. Funct. Mater.* **32**, 2207096.

[13] Zheng Y, Li X, Zheng M L, Cheng G, Zi Y L, Cheng S B, Cui H Z and Li X Y. 2024. MoSe₂ enhanced raindrop triboelectric nanogenerators and its energy conversion analysis. *Adv. Funct. Mater.* **34**, 2307669.

[14] Shan C C, Li K X, Cheng Y T and Hu C G. 2023. Harvesting environment mechanical energy by direct current triboelectric nanogenerators. *Nano-Micro Lett.* **15**, 127.

[15] Hu Y C, Qiu H J, Sun Q J, Wang Z L and Xu L. 2023. Wheel-structured triboelectric nanogenerators with hyperelastic networking for high-performance wave energy harvesting. *Small Methods* **7**, 2300582.

[16] Zhao X J, Wang H L, Wang Z L and Wang J. 2024. Nanocomposite electret layer improved long-term stable solid–liquid contact triboelectric nanogenerator for water wave energy harvesting. *Small* **20**, 2310023.

- [17] Liang X, Liu S J, Yang H B and Jiang T. 2023. Triboelectric nanogenerators for ocean wave energy harvesting: unit integration and network construction. *Electronics* **12**, 225.
- [18] Miao X, Yang H X, Li Z K, Cheng M F, Zhao Y L, Wan L Y, Yu A F and Zhai J Y. 2024. A columnar multi-layer sliding triboelectric nanogenerator for water wave energy harvesting independent of wave height and direction. *Nano Res.* **17**, 3029-3034.
- [19] Zhong J W, Zhong Q Z, Fan F R, Zhang Y, Wang S H, Hu B, Wang Z L and Zhou J. 2013. Finger typing driven triboelectric nanogenerator and its use for instantaneously lighting up LEDs. *Nano Energy* **2**, 491-497.
- [20] Lin Z H, Cheng G, Lin L, Lee S and Wang Z L. 2013. Water–solid surface contact electrification and its use for harvesting liquid-wave energy. *Angew. Chem. Int. Ed.* **52**, 12545-12549.
- [21] Choi D, Lee S, Park S M, Cho H, Hwang W and Kim D S. 2015. Energy harvesting model of moving water inside a tubular system and its application of a stick-type compact triboelectric nanogenerator. *Nano Res.* **8**, 2481-2491.
- [22] Chen J, Guo H Y, Zheng J G, Huang Y Z, Liu G L, Hu C G and Wang Z L. 2016. Self-powered triboelectric micro liquid/gas flow sensor for microfluidics. *ACS Nano* **10**, 8104-8112.
- [23] Wang Z L. 2017. Catch wave power in floating nets. *Nature* **542**, 159-160.
- [24] Xu W H *et al.* 2020. A droplet-based electricity generator with high instantaneous power density. *Nature* **578**, 392-396.
- [25] Tan L M, Zeng Q X, Xu F, Zhao Q, Chen A, Wang T Y, Tao X M, Yang Y C and Wang X. 2024. Controllable manipulation of large-volume droplet on non-slippery surfaces based on triboelectric contactless charge injection. *Adv. Mater.* **36**, 2313878.
- [26] Zhang X M, Yang Q X, Ji P Y, Wu Z F, Li Q Y, Yang H K, Li X C, Zheng G C, Xi Y and Wang Z L. 2022. Modeling of liquid-solid hydrodynamic water wave energy harvesting system based on triboelectric nanogenerator. *Nano Energy* **99**, 107362.
- [27] Liang X, Liu Z R, Feng Y W, Han J J, Li L L, An J, Chen P F, Jiang T and Wang Z L. 2021. Spherical triboelectric nanogenerator based on spring-assisted swing structure for effective water wave energy harvesting. *Nano Energy* **83**, 105836.
- [28] Xu W, Yang J Y, Liu S S, Meng Y, Feng D, Jia L J, Liu S D, Wang B L and Li X H. 2021. An instantaneous discharging liquid-solid triboelectric nanogenerator (IDLS-TENG) with boosted peak power output. *Nano Energy* **86**, 106093.
- [29] Dong J N, Fan F R and Tian Z Q. 2021. Droplet-based nanogenerators for energy harvesting and self-powered sensing. *Nanoscale* **13**, 17290-17309.
- [30] Choi D *et al.* 2023. Recent advances in triboelectric nanogenerators: from technological progress to commercial applications. *ACS Nano* **17**, 11087-11219.
- [31] Wu H, Wang Z K and Zi Y L. 2021. Multi-mode water-tube-based triboelectric nanogenerator designed for low-frequency energy harvesting with ultrahigh volumetric charge density. *Adv. Energy Mater.* **11**, 2100038.
- [32] Cui X, Nie J H and Zhang Y. 2024. Recent advances in high charge density triboelectric nanogenerators. *Int. J. Extrem. Manuf.* **6**, 042001.
- [33] Lee D, Chae J, Cho S, Kim J W, Ahmad A, Karim M R, La M, Park S J and Choi D. 2024. Bidirectional rotating direct-current triboelectric nanogenerator with self-adaptive mechanical switching for harvesting reciprocating motion. *Int. J. Extrem. Manuf.* **6**, 045502.
- [34] Xu C Q, Fu X P, Li C Y, Liu G X, Gao Y Y, Qi Y C, Bu T Z, Chen Y F, Wang Z L and Zhang C. 2022. Raindrop energy-powered autonomous wireless hyetometer based on liquid–solid contact

1
2
3 electrification. *Microsyst. Nanoeng.* **8**, 30.

4 [35] Peng J L, Zhang L Q, Liu Y, Xu C G, Yang D, Sun X, Feng Y G, Feng M, Sun W X and
5 Wang D A. 2022. New cambered-surface based drip generator: a drop of water generates 50 μ A current
6 without pre-charging. *Nano Energy* **102**, 107694.

7 [36] Gao Z Q, Wu S K, Wei Y H, Ibrahim M, Abdelhamid H N, Jiang G Y, Cao J, Sun X H and
8 Wen Z. 2024. Holistic and localized preparation methods for triboelectric sensors: principles,
9 applications and perspectives. *Int. J. Extrem. Manuf.* **6**, 052002.

10 [37] Liu X, Yu A F, Qin A M and Zhai J Y. 2019. Highly integrated triboelectric nanogenerator
11 for efficiently harvesting raindrop energy. *Adv. Mater. Technol.* **4**, 1900608.

12 [38] Dong Y, Wang N N, Yang D, Wang J, Lu W L and Wang D A. 2023. Robust solid-liquid
13 triboelectric nanogenerators: mechanisms, strategies and applications. *Adv. Funct. Mater.* **33**, 2300764.

14 [39] Liu G L, Xiao L F, Chen C Y, Liu W L, Pu X J, Wu Z Y, Hu C G and Wang Z L. 2020. Power
15 cables for triboelectric nanogenerator networks for large-scale blue energy harvesting. *Nano Energy*
16 **75**, 104975.

17 [40] Liu C Y and Bard A J. 2009. Electrons on dielectrics and contact electrification. *Chem. Phys.*
18 *Lett.* **480**, 145-156.

19 [41] Dai S F, Li X J, Jiang C M, Ping J F and Ying Y B. 2023. Triboelectric nanogenerators for
20 smart agriculture. *InfoMat* **5**, e12391.

21 [42] Xu W H, Song Y X, Xu R X and Wang Z K. 2021. Electrohydrodynamic and hydroelectric
22 effects at the water–solid interface: from fundamentals to applications. *Adv. Mater. Interfaces* **8**,
23 2000670.

24 [43] Zhu G, Su Y J, Bai P, Chen J, Jing Q S, Yang W Q and Wang Z L. 2014. Harvesting water
25 wave energy by asymmetric screening of electrostatic charges on a nanostructured hydrophobic thin-
26 film surface. *ACS Nano* **8**, 6031-6037.

27 [44] Xu X T, Wang Y L, Li P Y, Xu W H, Wei L, Wang Z K and Yang Z B. 2021. A leaf-mimic
28 rain energy harvester by liquid-solid contact electrification and piezoelectricity. *Nano Energy* **90**,
29 106573.

30 [45] Tang Z, Lin S Q and Wang Z L. 2021. Quantifying contact-electrification induced charge
31 transfer on a liquid droplet after contacting with a liquid or solid. *Adv. Mater.* **33**, 2102886.

32 [46] Wang X J, Zhang J Y, Liu X, Lin S Q and Wang Z L. 2023. Studying the droplet sliding
33 velocity and charge transfer at a liquid–solid interface. *J. Mater. Chem. A* **11**, 5696-5702.

34 [47] Song O, Cho Y, Cho S Y and Kang J. 2024. Solution-processing approach of nanomaterials
35 toward an artificial sensory system. *Int. J. Extrem. Manuf.* **6**, 052001.

36 [48] Solares-Bockmon C *et al.* 2022. Generalized dynamic junction theory to resolve the
37 mechanism of direct current generation in liquid-solid interfaces. *Nano Energy* **99**, 107364.

38 [49] Wang K Q and Li J J. 2021. Electricity generation from the interaction of liquid–solid
39 interface: a review. *J. Mater. Chem. A* **9**, 8870-8895.

40 [50] Li Z K, Yu A F, Zhang Q and Zhai J Y. 2024. Recent advances in fabricating high-
41 performance triboelectric nanogenerators via modulating surface charge density. *Int. J. Extrem. Manuf.*
42 **6**, 052003.

43 [51] Wei X L, Zhao Z H, Zhang C G, Yuan W, Wu Z Y, Wang J and Wang Z L. 2021. All-weather
44 droplet-based triboelectric nanogenerator for wave energy harvesting. *ACS Nano* **15**, 13200-13208.

45 [52] Zhang Q *et al.* 2021. A single-droplet electricity generator achieves an ultrahigh output over
46 100 V without pre-charging. *Adv. Mater.* **33**, 2105761.

- [53] Xu X T, Li P Y, Ding Y T, Xu W H, Liu S Y, Zhang Z M, Wang Z K and Yang Z B. 2022. Droplet energy harvesting panel. *Energy Environ. Sci.* **15**, 2916-2926.
- [54] Zhang Y H, Li Y Y, Cheng R W, Shen S, Yi J, Peng X, Ning C, Dong K and Wang Z L. 2022. Underwater monitoring networks based on cable-structured triboelectric nanogenerators. *Research* **2022**, 9809406.
- [55] Xiao X, Liu L, Xi Z Y, Yu H Y, Li W X, Wang Q Y, Zhao C, Huang Y and Xu M Y. 2023. Research on an optimized quarter-wavelength resonator-based triboelectric nanogenerator for efficient low-frequency acoustic energy harvesting. *Nanomaterials* **13**, 1676.
- [56] Zhang B S, Jiang Y C, Ren T C, Chen B J, Zhang R Y and Mao Y C. 2024. Recent advances in nature inspired triboelectric nanogenerators for self-powered systems. *Int. J. Extrem. Manuf.* **6**, 062003.
- [57] Cao X L, Zhou H L, Zhou Y X, Hu Y R, Wang Y Y, Wang Z L and Sun Q J. 2023. High performance rotary-structured triboelectric-electromagnetic hybrid nanogenerator for ocean wind energy harvesting. *Adv. Mater. Technol.* **8**, 2300327.
- [58] Hao Y C *et al.* 2021. Metal-organic framework membranes with single-atomic centers for photocatalytic CO₂ and O₂ reduction. *Nat. Commun.* **12**, 2682.
- [59] Lin Z H, Cheng G, Lee S, Pradel K C and Wang Z L. 2014. Harvesting water drop energy by a sequential contact-electrification and electrostatic-induction process. *Adv. Mater.* **26**, 4690-4696.
- [60] Zheng Y, Liu T, Wu J P, Xu T T, Wang X D, Han X, Cui H Z, Xu X F, Pan C F and Li X Y. 2022. Energy conversion analysis of multilayered triboelectric nanogenerators for synergistic rain and solar energy harvesting. *Adv. Mater.* **34**, 2202238.
- [61] Wu H, Chen Z F, Xu G Q, Xu J B, Wang Z K and Zi Y L. 2020. Fully biodegradable water droplet energy harvester based on leaves of living plants. *ACS Appl. Mater. Interfaces* **12**, 56060-56067.
- [62] Chen Y *et al.* 2021. Interfacial laser-induced graphene enabling high-performance liquid–solid triboelectric nanogenerator. *Adv. Mater.* **33**, 2104290.
- [63] Zhao L L, Liu L Q, Yang X Y, Hong H X, Yang Q M, Wang J W and Tang Q W. 2020. Cumulative charging behavior of water droplet driven freestanding triboelectric nanogenerators toward hydrodynamic energy harvesting. *J. Mater. Chem. A* **8**, 7880-7888. .

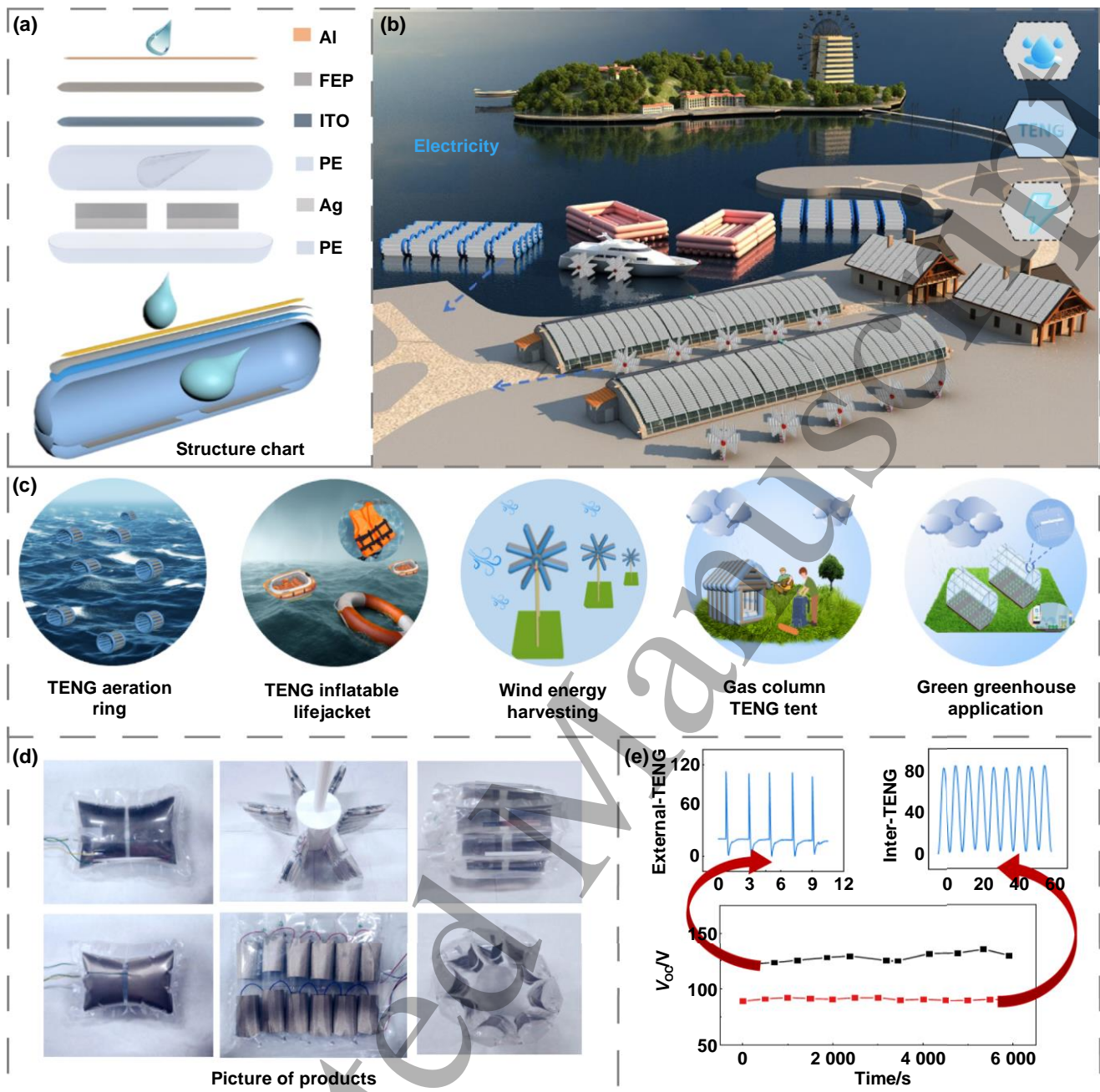


Figure 1. Basic structure, performance and application scenarios of LS-TENG. (a) Front expansion and side structure of combined LS-TENG. (b)-(c) Application scenario of LS-TENG. (d) Schematic diagrams of different designs based on the LS-TENG. (e) Cyclic stability of output voltage for both the inner LS-TENG and external LS-TENG.

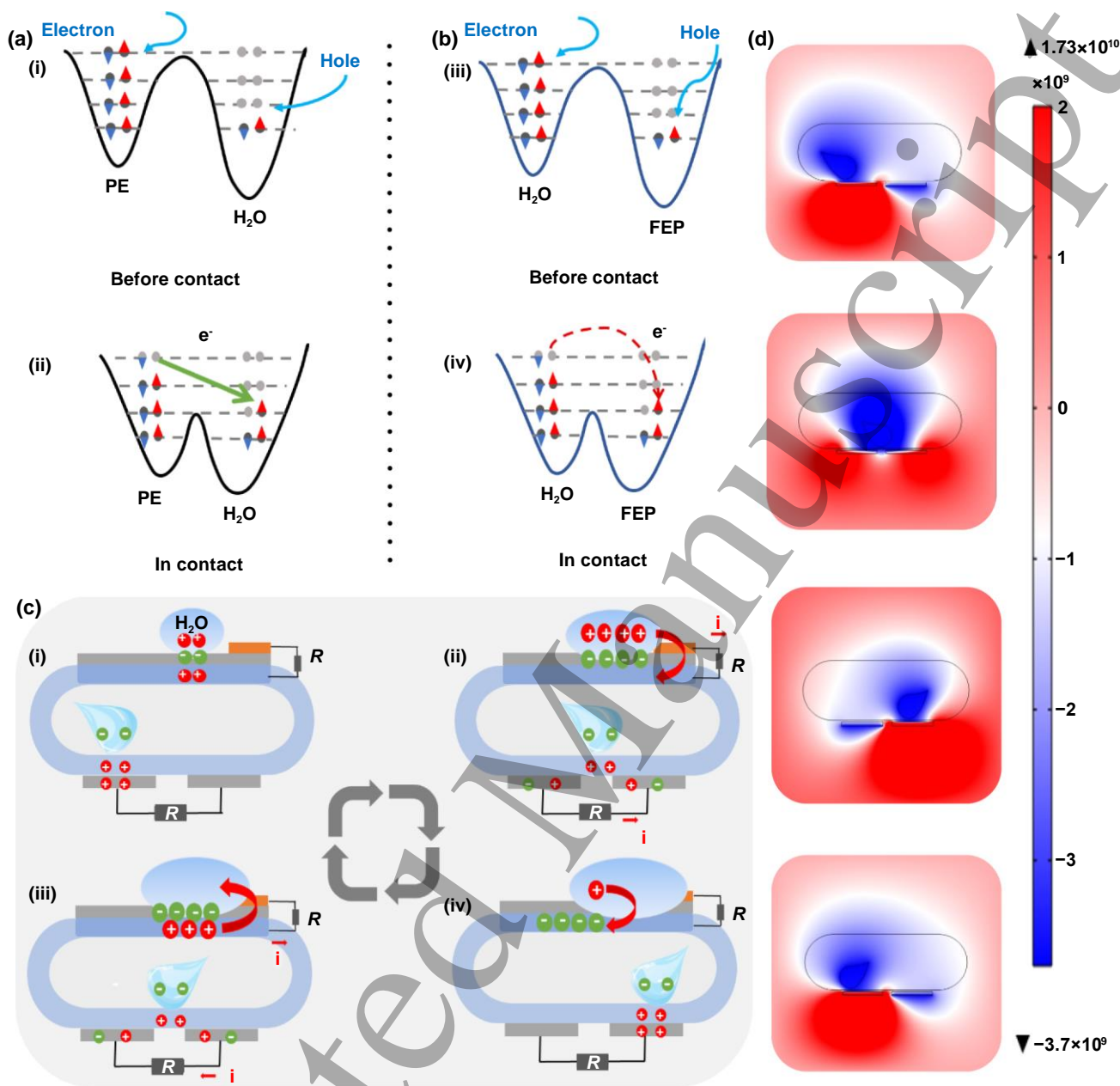


Figure 2. Electronic transition and working principle of LS-TENG. (a) Schematic illustration of the electron transfer process from PE film to water for the inner LS-TENG. (b) Schematic diagram of electron transfer process from water to FEP membrane for the external LS-TENG. (c) Schematic diagram of the working mechanism for the combined LS-TENG. (d) The variation of electrical potential distribution during internal water movement.

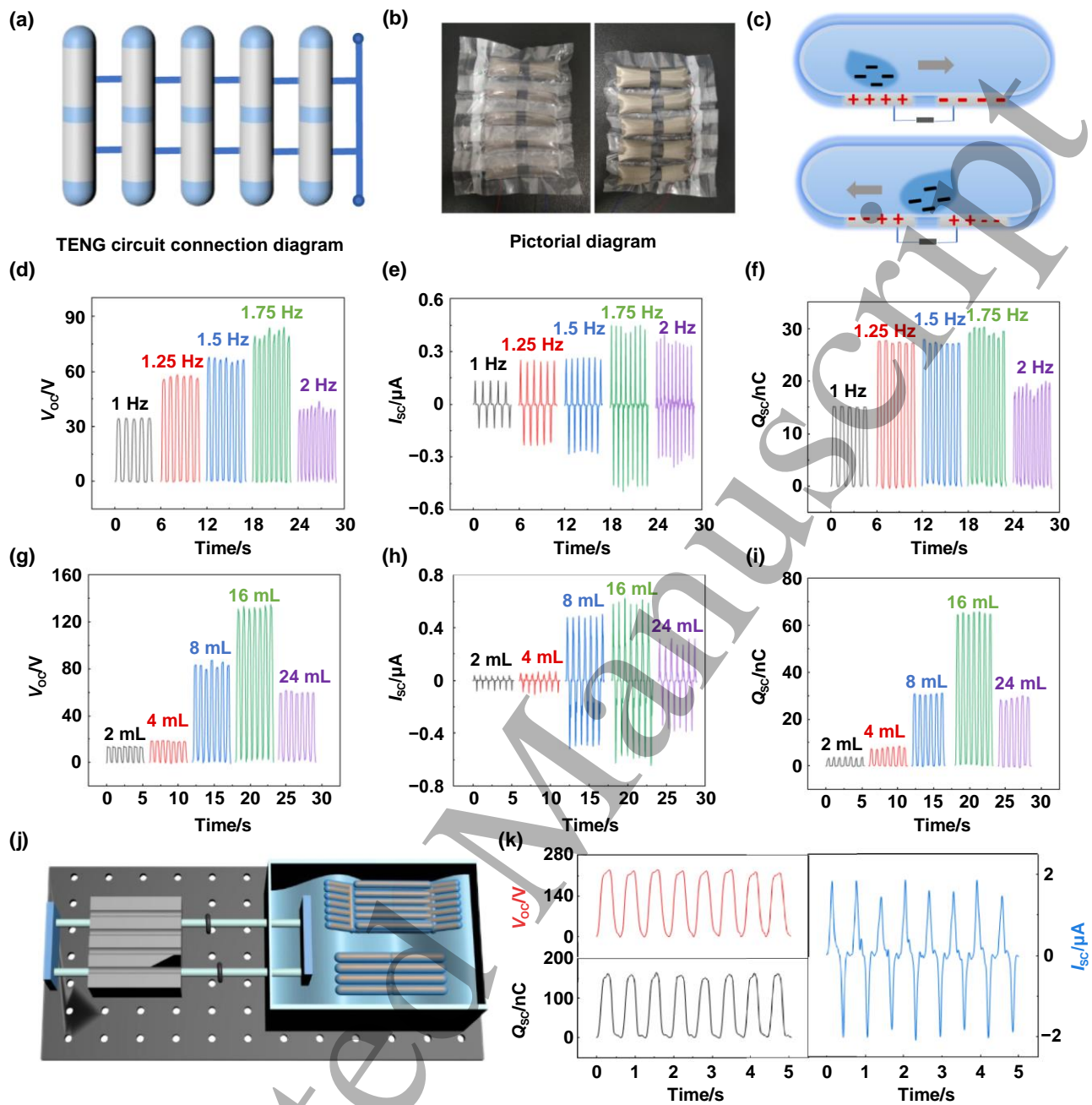


Figure 3. Internal LS-TENG impact factor test. (a) Diagram for internal circuit connection. (b) Photo image for internal circuit connection. (c) Charge transfer mechanism for inner LS-TENG. (d)-(f) Single inflatable unit output of V_{OC} , I_{OC} , Q_{SC} under different working frequencies. (g)-(i) The output performances are directly related to the amount of injected water. (j) Schematic diagram of the working process for an inflatable raft constructed from LS-TENGs. (k) The total output performance of the LS-TENGs for constructing the inflatable raft.

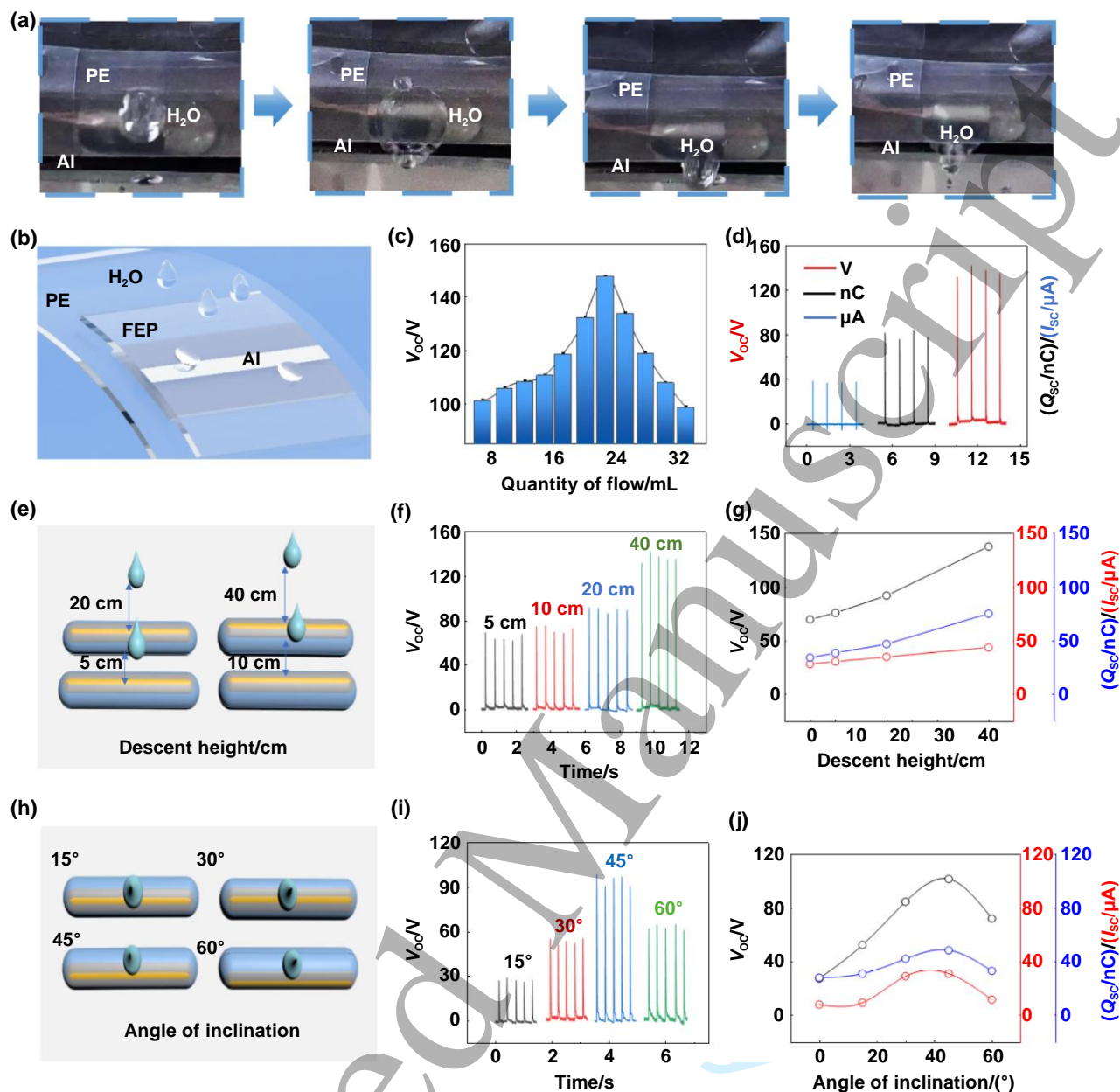


Figure 4. External LS-TENG impact factor testing. (a) The dynamic dropping process of a water droplet for the external LS-TENG. (b) Schematic diagram of the external LS-TENG. (c) Influence of the droplet volume on the output performance. (d) Maximum output performance of a single droplet. (e), (h) Schematic diagram of droplet falling at different heights and angles. (f)-(g) Influence of different falling heights (5, 10, 20, 40 cm) on the output performances. (i)-(j) Influence of different falling angles (15°, 30°, 45°, 60°) on the output performances.

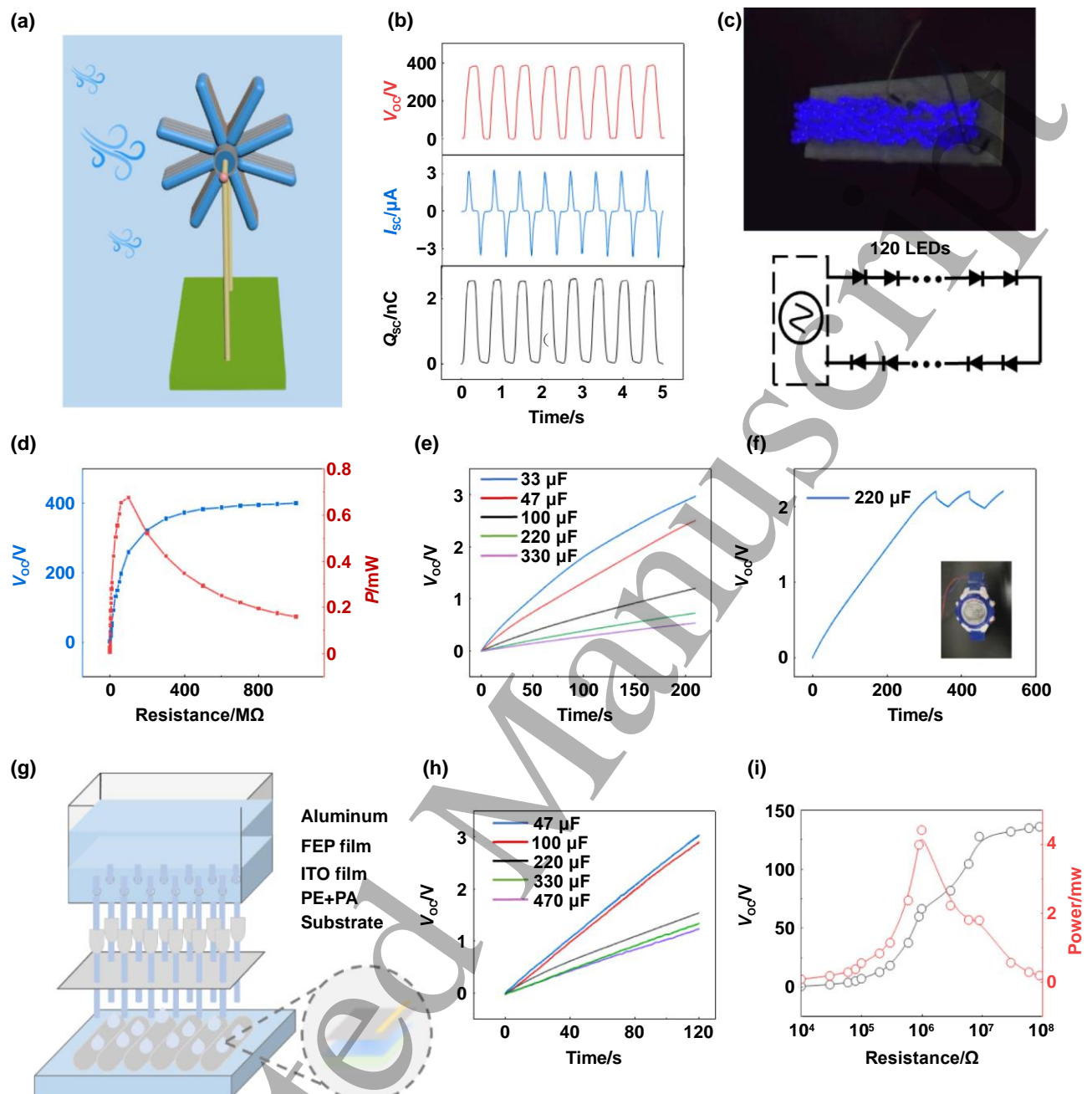


Figure 5. LS-TENG electrical performance test. (a) Schematic diagram of integrated windmill structure. (b) Output performance of the integrated windmill. (c) The windmill structured TENG can light up 120 LEDs. (d) The relationship between voltage and power of the inner LS-TENG vs. different load resistances. (e) Charging curves for different capacitors by using the windmill structured TENG. (f) Using the windmill TENG to drive an electronic watch. (g) Custom testing facility for the external LS-TENGs array. (h) Charging curves for different capacitors by a single external LS-TENG. (i) The relationship between the output voltage and power of the external LS-TENG vs. different load resistances.

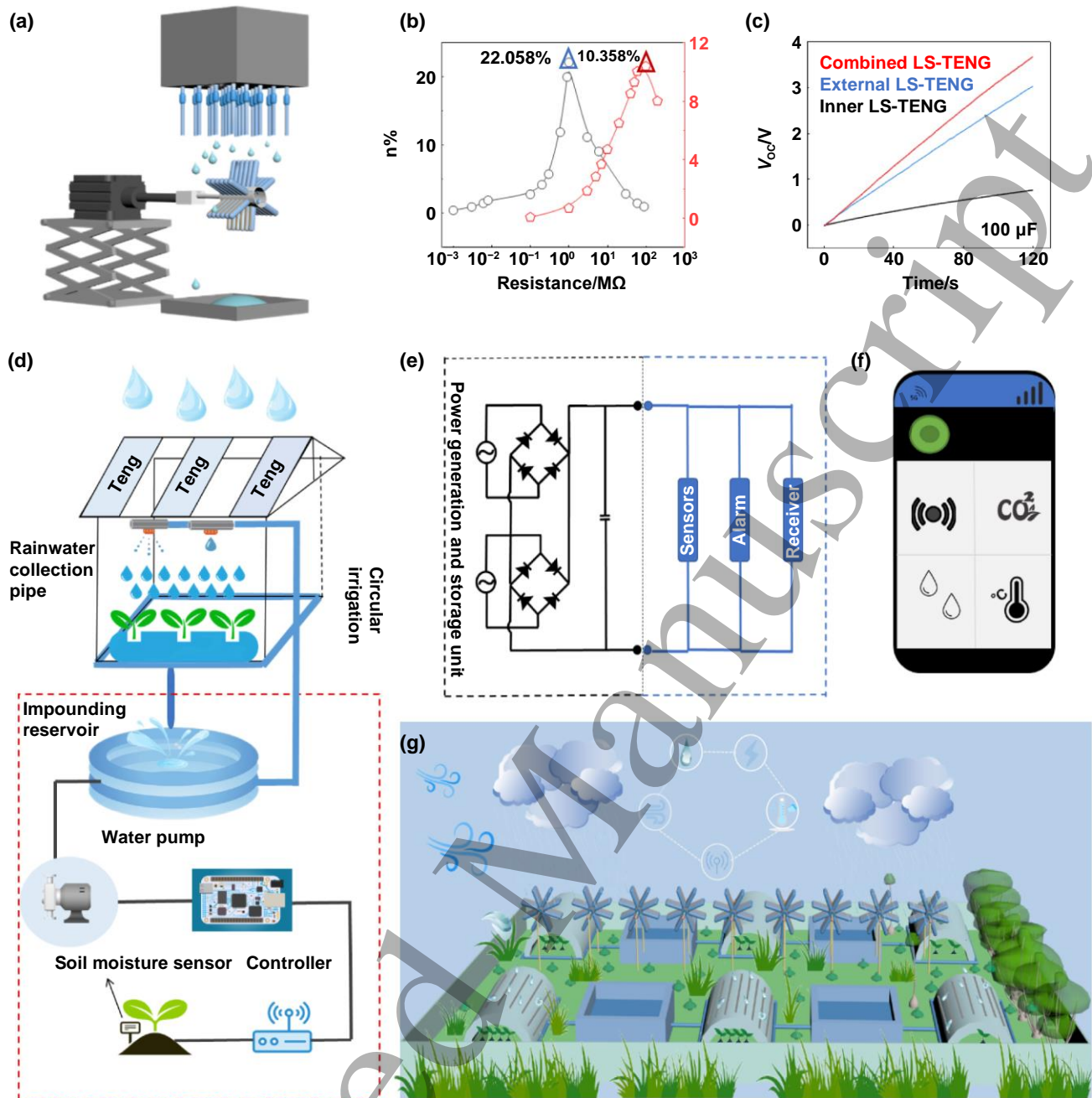


Figure 6. Performance and self-irrigation cycle scenario display. (a) Demonstration of the windmill structure to utilize the combined LS-TENG for harvesting both internal and external mechanical energy. (b) Conversion efficiency of inner and external LS-TENGs under different loads. (c) Different charging curves for a $100 \mu F$ capacitor by inner LS-TENG, external LS-TENG, and combined LS-TENG (d) Schematic diagram of the proposed intelligent greenhouse with self-powered automatic irrigation system. (e)-(f) Circuit diagram of the self-powered system based on the combined LS-TENG. (g) Outlook of the combined LS-TENG in intelligent greenhouse applications.

1
2
3
4
5 Supporting information
6
7

8
9 **Constructing High-Performance and Versatile Liquid-Solid**
10
11 **Triboelectric Nanogenerator with Inflatable Columnar Units**
12
13
14

15
16 Lin Luo^{1,2}, Chao Liu^{1,2}, Rui Gu^{2,4}, Mingxia Chen^{2,3}, Yifei Wang^{2,4}, Nuo Xu^{1,2}, Yao Xiong^{2,4}, Jiahong Yang^{2,4},
17
18 Ziwei Huo^{2,4}, Yang Liu^{2,4}, Liang Wei^{1,2}, Zhong Lin Wang^{2,5*}, Qijun Sun^{1,2,4,5,6*}
19
20

21
22 ¹ Center on Nanoenergy Research, Institute of Science and Technology for Carbon Peak & Neutrality; Key
23
24 Laboratory of Blue Energy and Systems Integration (Guangxi University), Education Department of Guangxi
25
26 Zhuang Autonomous Region; School of Physical Science & Technology, Guangxi University, Nanning 530004,
27
28 China.
29

30 ² Beijing Institute of Nanoenergy and Nanosystems, Chinese Academy of Sciences, Beijing, 101400, China
31

32 ³ Center on Nanoenergy Research, School of Chemistry and Chemical Engineering, Guangxi University,
33
34 Nanning 530004, PR China
35

36 ⁴ School of Nanoscience and Technology, University of Chinese Academy of Sciences, Beijing, 100049, China
37

38 ⁵ Georgia Institute of Technology, Atlanta, GA, 30332, USA
39

40 ⁶ Shandong Zhongke Naneng Energy Technology Co., Ltd., Dongying, 257061, China
41
42
43

44
45 E-mail: sunqijun@binn.cas.cn, zhong.wang@mse.gatech.edu
46
47
48
49
50
51
52
53
54
55
56
57
58
59
60

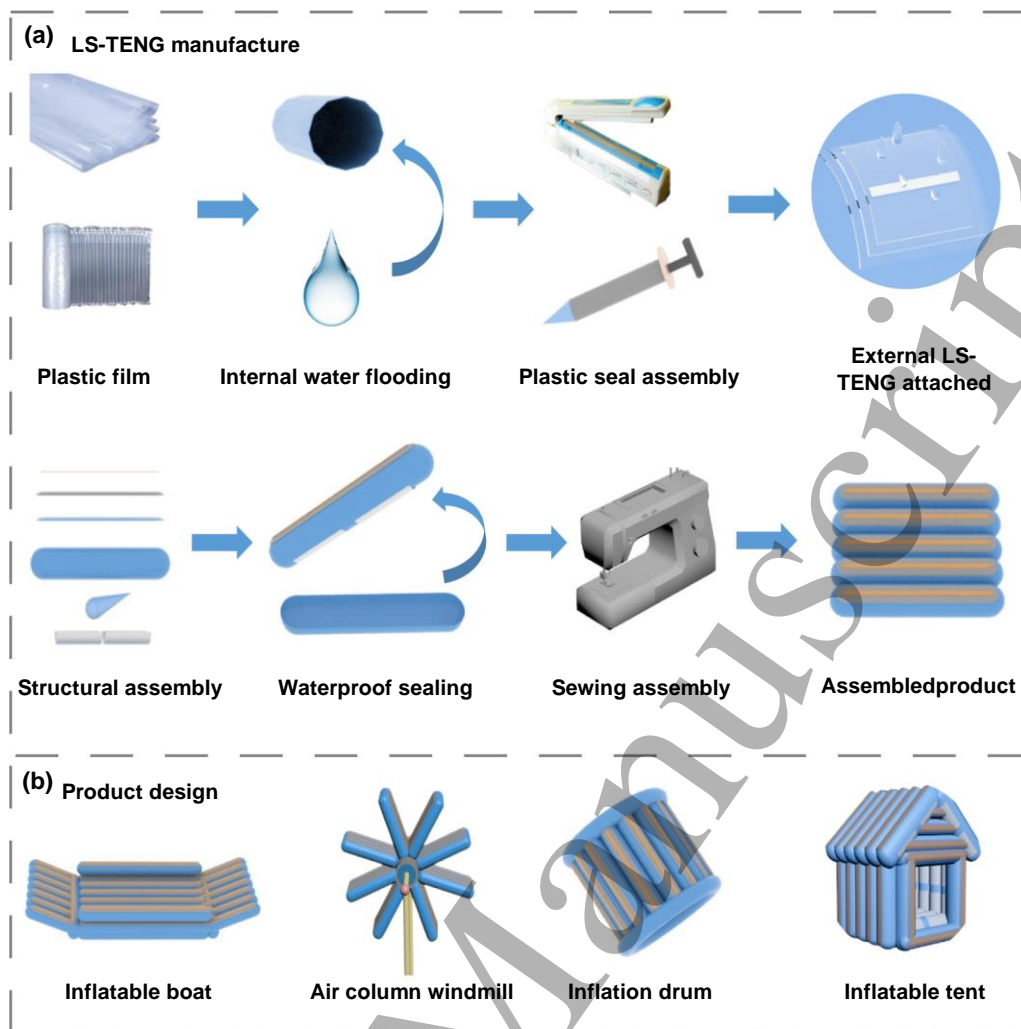


Figure S1. Manufacturing process for the liquid-solid triboelectric nanogenerator (LS-TENG) and diverse applications with the inflatable columnar LS-TENG units. (a) Fabrication process and steps of liquid-solid composite friction nanogenerator. (b) Design of application products of LS-TENG.

The fabrication process of the LS-TENG is illustrated in **Figure S1(a)**. First, polyethylene (PE) films were heat-shrunk into different specifications of air chamber styles, then a proportional amount of water was injected into them, and they were sealed using a sealing machine and then inflated using an inflator. The two pieces of silver cloth on the back of the inflated air chamber acted as electrodes, forming the internal LS-TENG. Next, the external LS-TENG structure was designed on the upper surface of the air chamber, and ITO (electrode), FEP film (friction layer), and Al strip (electrode) were attached in sequence to form the final combined LS-TENG. Finally, the back of the combined LS-TENG was waterproofed and sealed to form the final single LS-TENG structure. For the array assembly of the single LS-TENGs, we used sewing and heat-shrinking methods to combine them tightly together, and then designed them into different product structures for applications in various fields, as shown in **Figure S1(b)**.

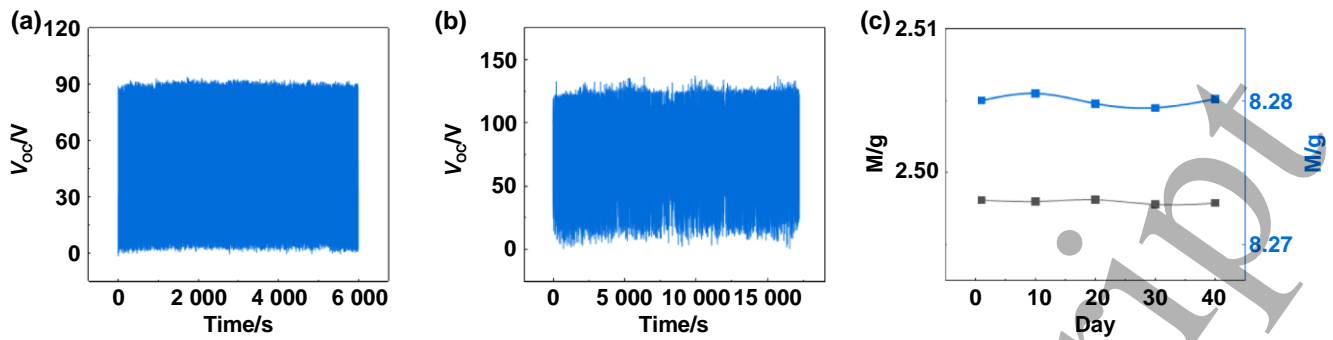


Figure S2. Cyclic stability and mass stability test diagram. (a)-(b) Cyclic stability of inner LS-TENG and external LS-TENG. (c) Quality stability of combined LS-TENG.

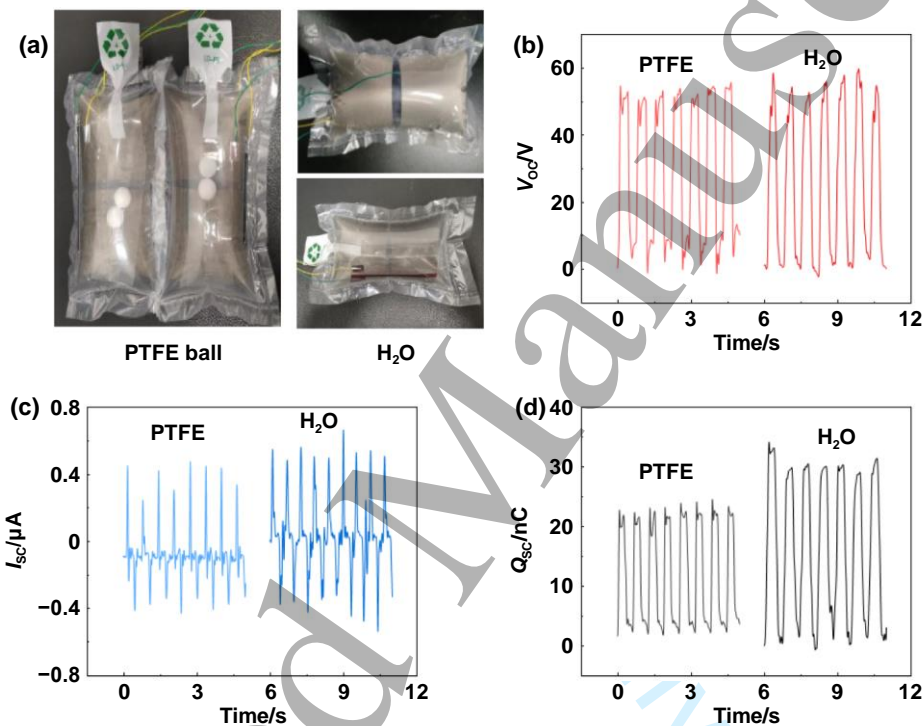


Figure S3. Output performance comparison of the inflatable structured TENGs with polytetrafluoroethylene (PTFE) spheres and H₂O as the inner friction materials. (a) The physical diagram of the aerated structure TENG with (PTFE) sphere and H₂O as internal friction materials. (b)-(d) Comparison of electrical output properties of two different materials.

We discuss the reason for the selection of triboelectric material within the inflatable column, as shown in **Figure S3**. By comparing the output performance of water and PTFE pellets as friction materials, it can be seen that water slightly outperforms PTFE spheres in all output metrics, while keeping the frequency, inflatable column, moving distance, and electrodes the same. PTFE spheres are also relatively expensive, which increases the cost for large-scale applications; considering all factors, water was selected as the

triboelectric material for this device.

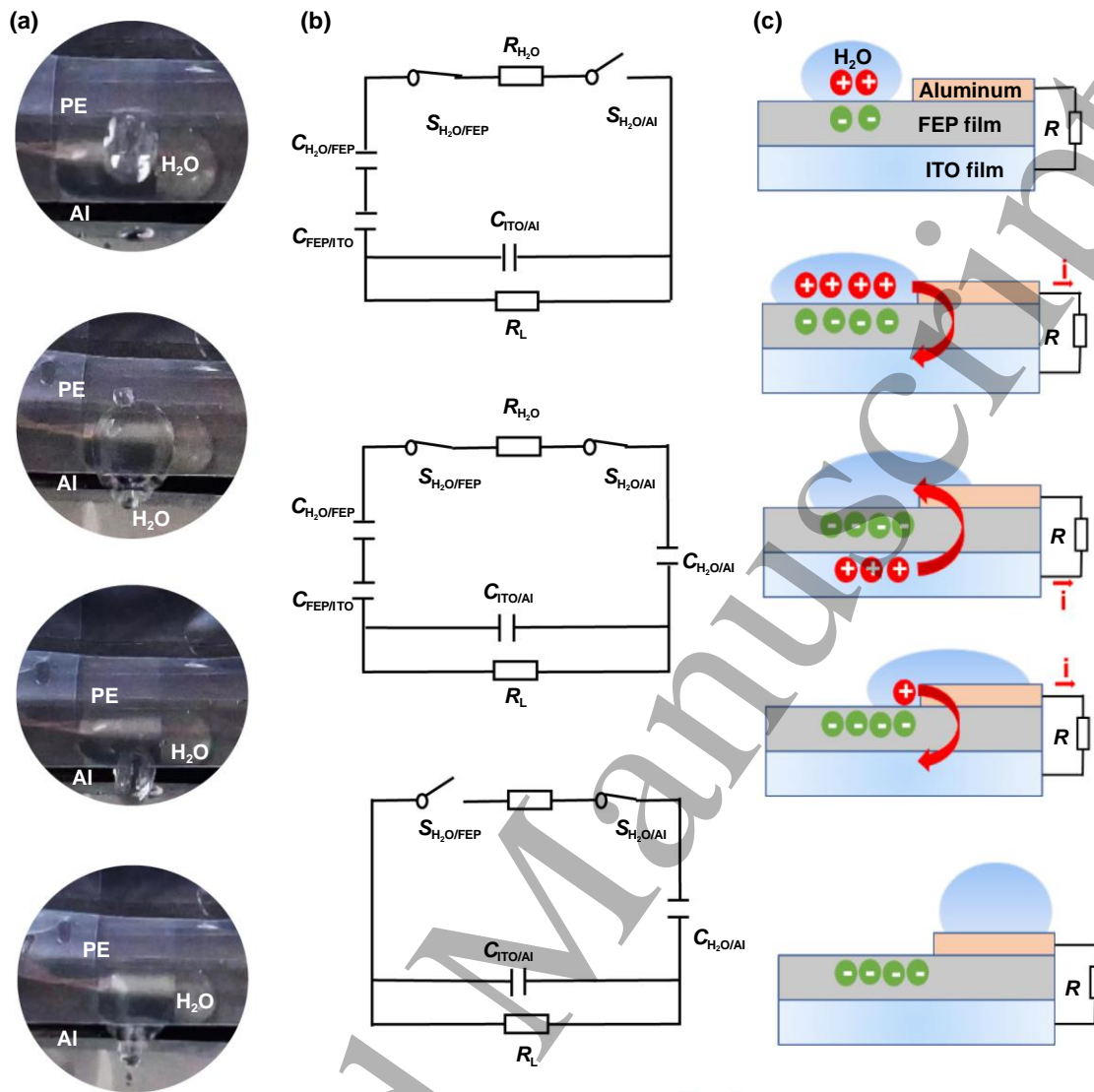


Figure S4. Equivalent circuit diagram and schematic diagram for different positions of droplets. (a) Actual picture of external LS-TENG water droplets at different locations. (b) Equivalent circuit diagram of droplet in different positions. (c) The working principle diagram of the droplet in different positions.

We assume that after the droplet comes into contact with Al, the droplet no longer accumulates positive triboelectric charges and the $C_{H_2O/Al}$ capacitor does not generate separated charges. According to Kirchhoff's voltage-current law, the whole process involved in (b) can be described as the following differential equations:

$$\frac{Q_0 - q(t)}{C_{H_2O/FEP}(t)} - \frac{dq(t)}{dt} R_D - \frac{q(t)}{C_{H_2O/Al}(t)} - U_{R_L}(t) - \frac{q(t)}{C_{FEP/ITO}(t)} = 0$$

$$\frac{dq(t)}{dt} - C_{ITO/Al} \frac{dU_{R_L}(t)}{dt} - \frac{U_{R_L}(t)}{R_L} = 0$$

$$q(t = 0) = 0$$

$$U_{R_L}(t = 0) = 0$$

$$C_{H2O/FEP}(t) = \frac{\varepsilon_D S_{FEP}(t)}{d_R}$$

$$C_{H2O/Al}(t) = \frac{\varepsilon_D S_{Al}(t)}{d_R}$$

$$C_{FEP/ITO}(t) = \frac{\varepsilon_F S_{FEP}(t)}{d_{FEP}}$$

$$C_{ITO/Al} = \frac{\varepsilon_F S_{Al-FEP}}{d_{FEP}}$$

where Q_0 denotes the accumulated positive charge of $C_{H2O/FEP}$ when the droplet contacts Al, $q(t)$ denotes the amount of charge transferred in the loop and represents the voltage across the load, and $\varepsilon U_{RL}(t)_D$ and ε_F denote the dielectric constants of the droplet and FEP, respectively. In addition, $S_{FEP}(t)$ and $S_{Al}(t)$ denote the contact area between the droplet and the FEP on the Al surface. S_{Al-FEP} denotes the area covered by Al on the FEP surface, d_R denotes the thickness of the bilayer, and d_{FEP} denotes the thickness of the FEP [52].

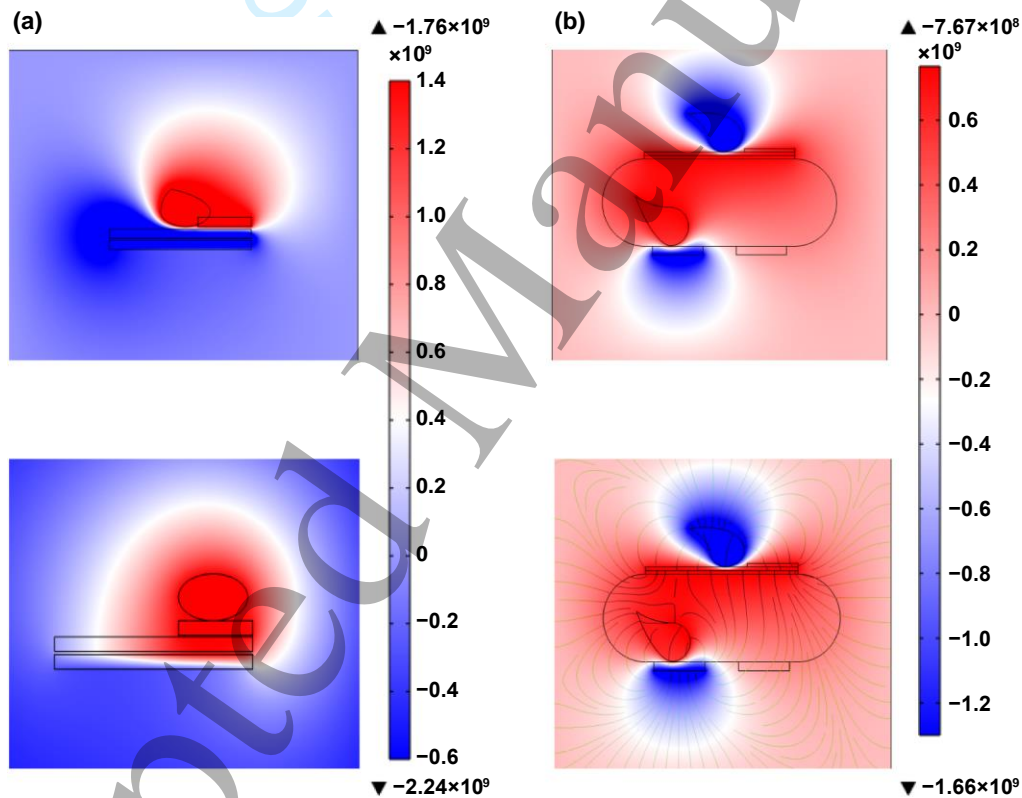


Figure S5. Potential distribution of external and combined LS-TENG. (a) Potential distribution diagram of external LS-TENG. (b) Potential distribution diagram of the combined LS-TENG.

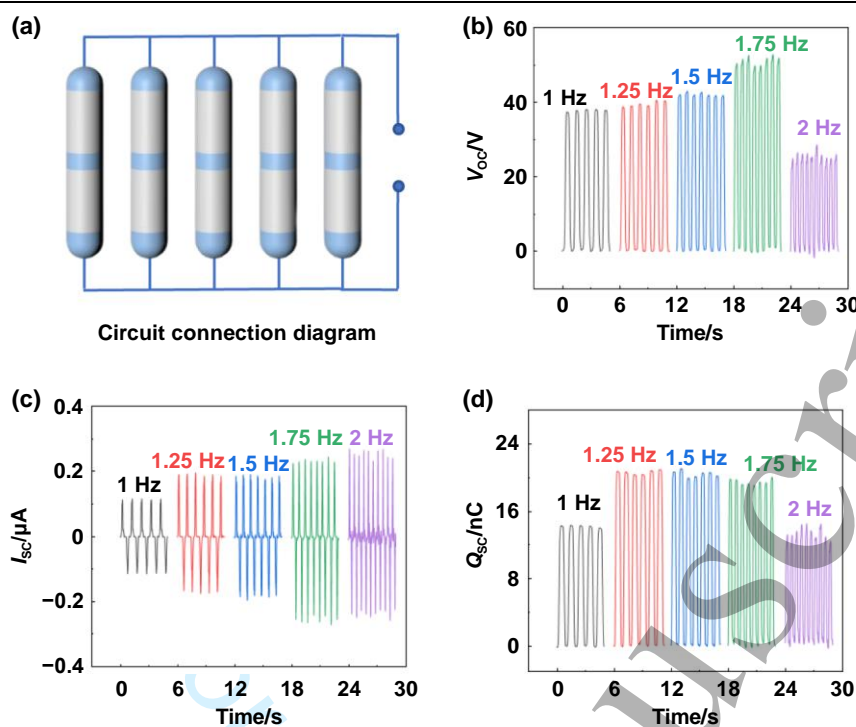


Figure S6. In-parallel circuit diagram and output performance of the inner LS-TENG. (a) Shunt circuit diagram of internal LS-TENG. (b)-(d) Comparison of parallel output performance of internal LS-TENG.

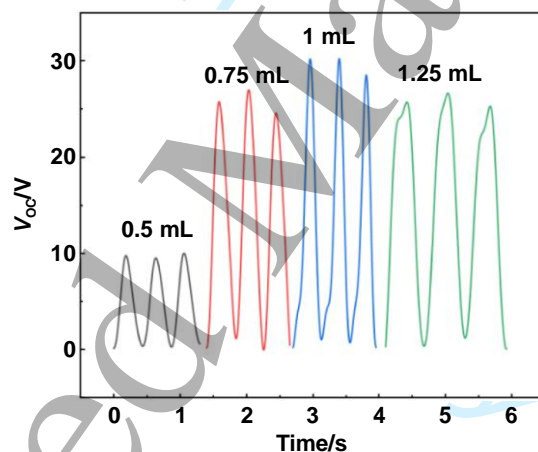


Figure S7. Characterization of different water injection volumes.

In **Figure S7**, we chose the volume of the air column to be about 9π , and observed the output performance under different liquid injection volumes through experiments. According to the results, we can clearly observe that the experiment shows the maximum output performance when the volume of injected liquid is 1 mL. Based on this result, we conclude that the optimal volume ratio of the air column to water is $1/9\pi$. This conclusion is reached through rigorous experimental design and data analysis, which is of great significance in guiding us to further optimize the experimental parameters and performance enhancement.

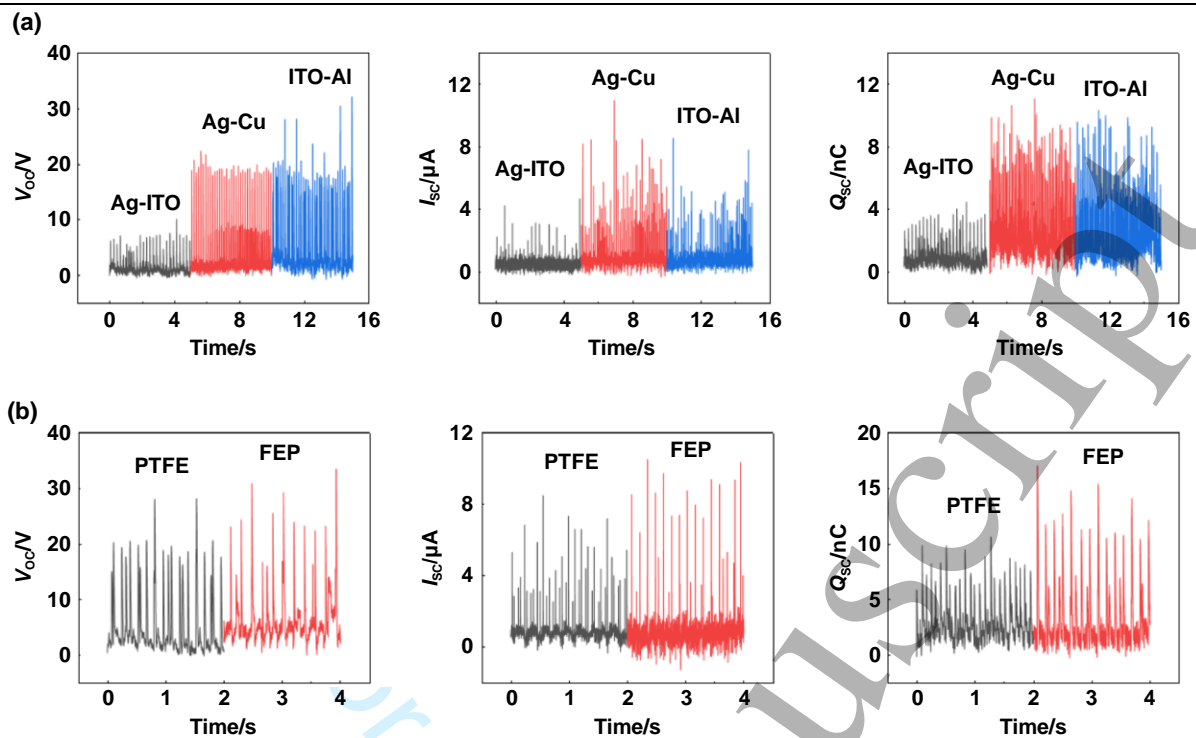


Figure S8. Comparison of LS-TENG output of different electrode types and different friction layers. (a) Comparison of the LS-TENG outputs with different types of electrodes. (b) Comparison of the LS-TENG outputs with different friction layers.

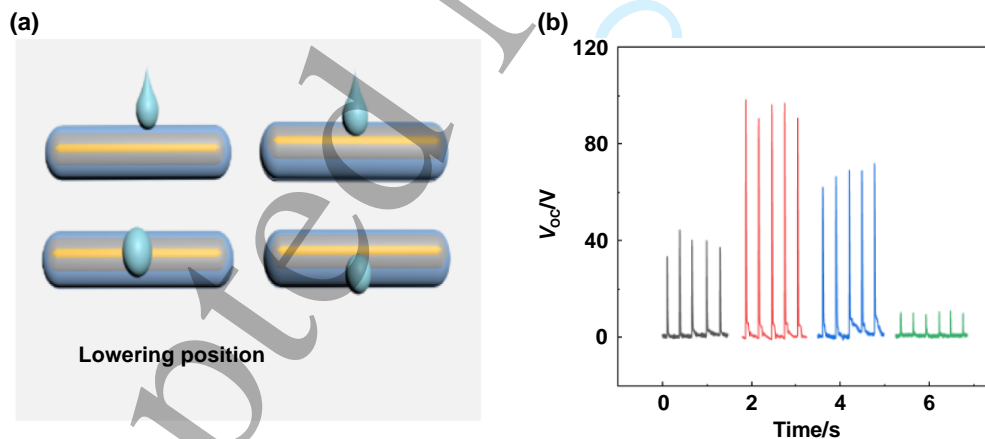


Figure S9. The model diagram of different droplet dropping positions and corresponding output signals. (a) A model diagram of the droplet in different positions. (b) Comparison of output performance of droplet at different positions.

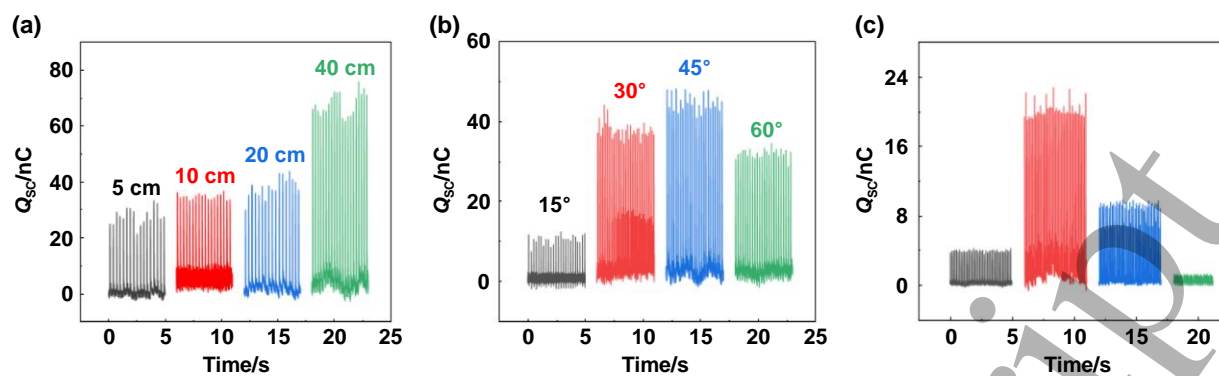


Figure S10. Transferred charges of the external LS-TENG at different falling heights, angles, and contact positions. (a) External LS-TENG droplets transfer charge at different falling heights. (b) Comparison of charge transfer of external LS-TENG water droplets at different contact angles. (c) Comparison of charge transfer at different contact positions of external LS-TENG water droplets.

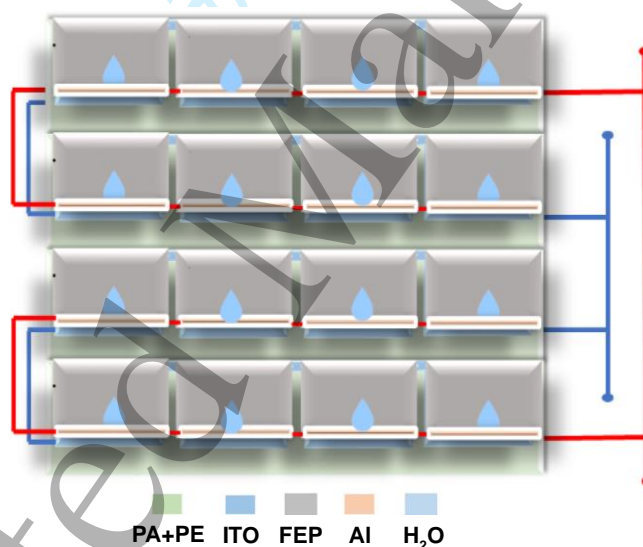


Figure S11. Circuit connection method for multiple external LS-TENGs.

The circuit in **Figure S11** is optimized for a specific function or performance by utilizing the characteristics of both series and parallel connections. Series connections are utilized to provide high voltage or high impedance characteristics while parallel connections are utilized to provide high current or low impedance characteristics. By rationally designing the circuit design and component parameters, it is possible to achieve flexible control and optimization of the circuit's voltage, current, impedance, and other parameters.

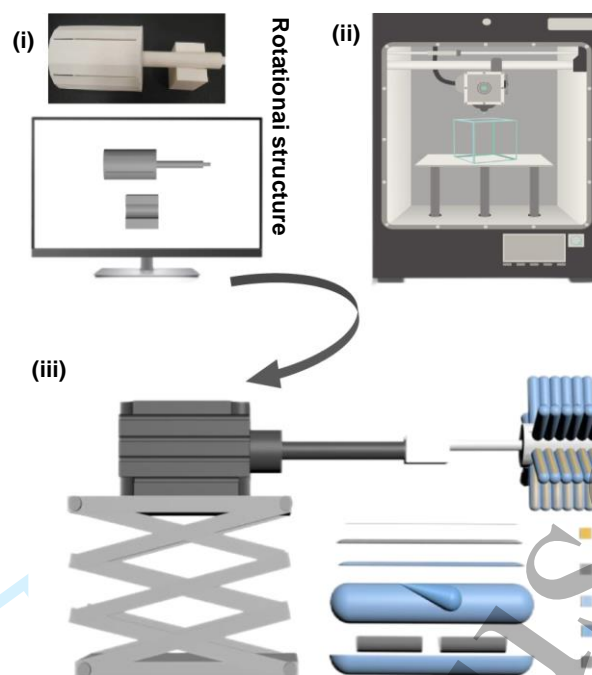


Figure S12. 3D printing and manufacturing of windmill with the combined LS-TENGs.

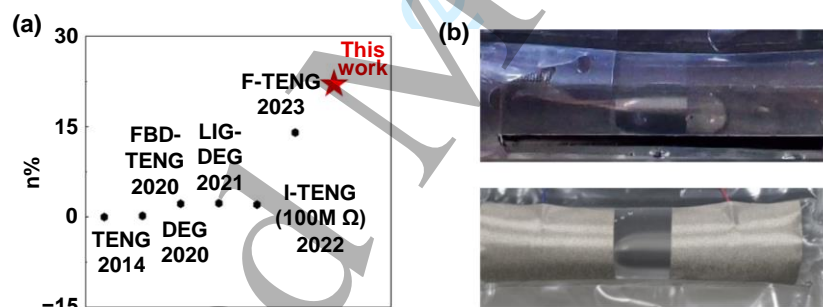


Figure S13. The actual LS-TENG diagram and the comparison of the transformation efficiency of droplet TENG over the years. (a) Comparative diagram of the conversion efficiency for droplet TENG over ten years. (b) Photo image of the LS-TENG.

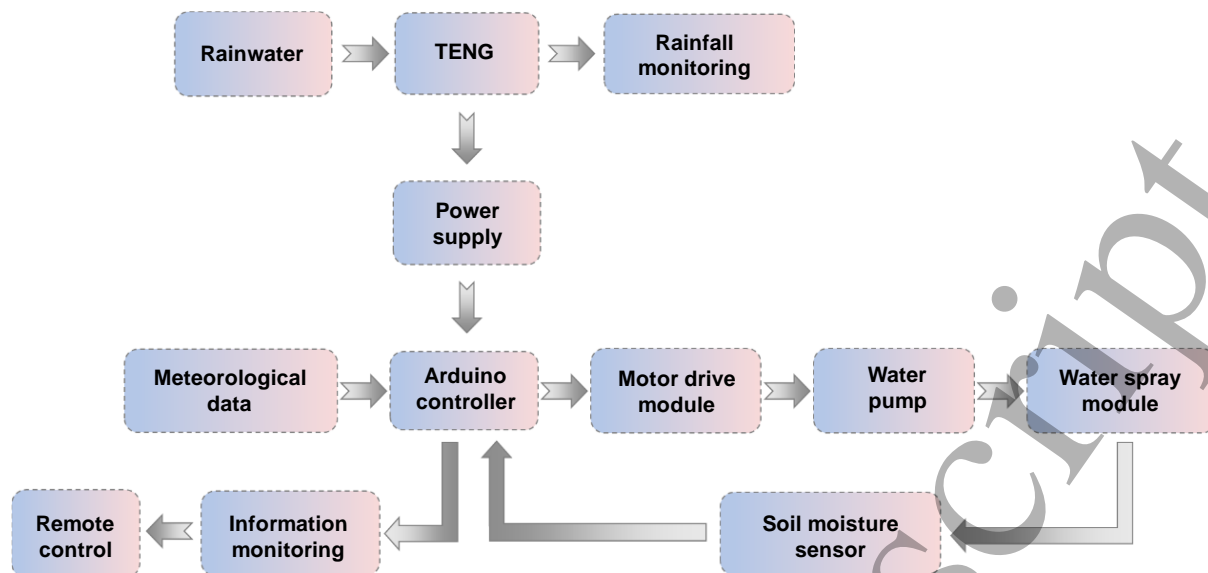


Figure S14. The flow chart of self-irrigation system.

Figure S14 shows in detail the complete flow chart of soil moisture sensing in a wetland self-irrigation system, in which TENG acts as an energy supply component and rainfall monitoring sensor. The flow chart illustrates the entire process from soil moisture monitoring to automatic control of irrigation in a highly specialized manner. This process is designed to achieve accurate perception and efficient management of soil water content in the wetland environment to ensure the continued health and stability of the wetland ecosystem. **Figure S14** defines the core components of the system, i.e., the soil moisture sensor, the data acquisition and processing unit, and the irrigation control actuator. These elements work together to form the intelligent monitoring and control network of wetland self-irrigation system. At the beginning of the flow diagram, soil moisture sensors are deployed at key monitoring points in the wetlands. These sensors use a high-precision fork probe design with a bare conductor acting as a variable resistor that dynamically adjusts the resistance value based on the moisture content in the soil. When the soil moisture increases, the electrical conductivity increases, resulting in a decrease in electrical resistance. On the contrary, the resistance of dry soil increases. This change is converted into a measurable voltage signal by an electronic module, which enables real-time monitoring of soil moisture. The data acquisition and processing unit then receive an analog or digital signal from the soil moisture sensor. The unit has a high precision ADC (analog-to-digital converter) and a microprocessor, which filters, amplifies, and digitizes the received signal to eliminate noise interference and improve data accuracy. At the same time, software algorithms were used to further analyze the processed data, calculate the current soil moisture state, and compare it with the preset humidity threshold. Based on the results of real-time soil moisture data compared to preset thresholds, irrigation control actuators automatically make

irrigation decisions. When the soil moisture is below the lower limit, the system determines that it is in a state of water shortage, and then triggers the irrigation program to start the irrigation operation by controlling the actuator such as the solenoid valve or the pump to replenish the required water for the wetland. On the contrary, if the soil moisture is within the appropriate range or exceeds the upper limit, the system maintains the current state or shuts down irrigation to avoid water waste or wetland ecological damage caused by excessive irrigation.

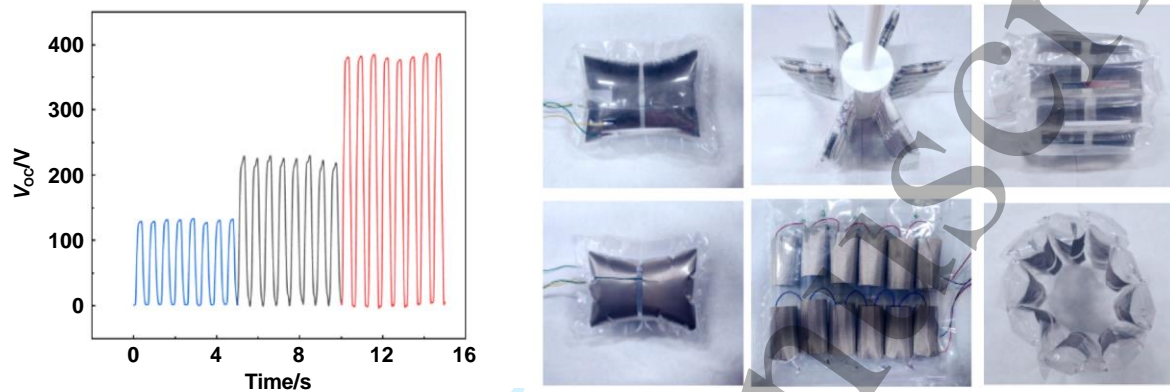


Figure S15. Characterization measurements under different energies (biokinetic energy, hydro energy, and wind energy).

In **Figure S15**, this study provides an insight into the potential for application in multiple environments and design versatility by comparing the performance of different structural designs from different energy sources.

By systematically comparing and analyzing different structures for biokinetic, hydroelectric, and wind energy, we are able to more comprehensively assess their performance strengths and weaknesses under specific environmental conditions, and provide useful references for the development of future renewable energy technologies. This study not only demonstrates the feasibility of various structural designs in practical applications, but also highlights their suitability and flexibility in different environments. This finding provides important guidance and insights for the design of more efficient and sustainable biokinetic, hydroelectric, and wind energy conversion systems.

Our findings are not only important for deepening the understanding of renewable energy technologies, but also provide valuable empirical support for interdisciplinary research and engineering applications. This research provides new perspectives for future development and innovation in the field of renewable energy and facilitates its significant potential in practical applications.

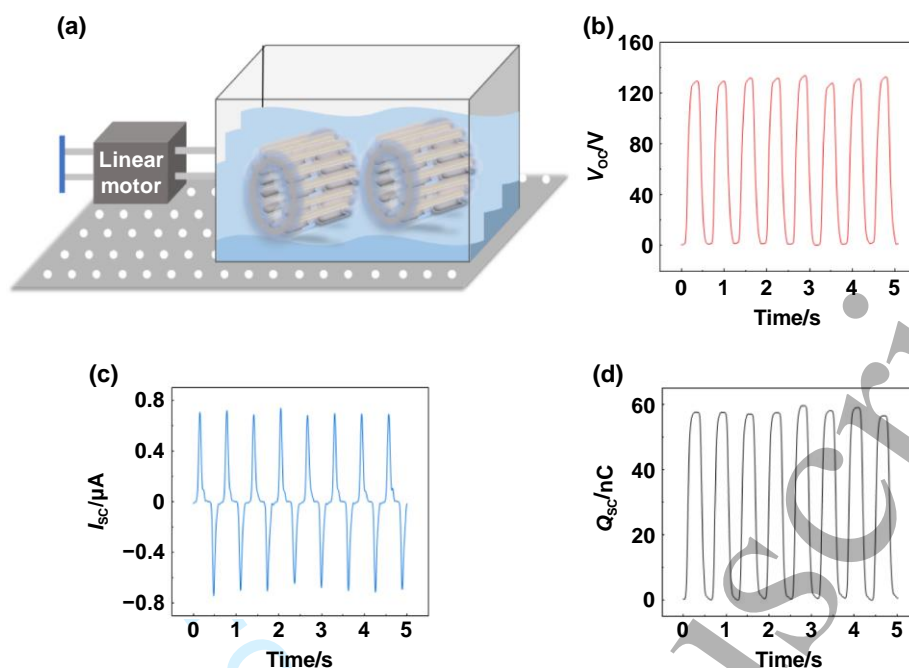


Figure S16. Water wave energy harvesting by the combined LS-TENG. (a) Application test and demonstration of liquid-solid LS-TENG of drum structure. (b)-(d) Output performance diagram of LS-TENG of drum structure under regular water wave.

Figure S16(a) illustrates the architecture of a roller-shaped LS-TENG for simultaneous harvesting of rainfall and ocean wave energy; a single roller model was assembled using ten small-sized LS-TENGs (each with a volume of $48\pi \text{ cm}^3$). Its maximum output, driven by wave energy, was $V_{OC} = 133.43 \text{ V}$, $I_{SC} = 0.734 \mu\text{A}$, and $Q_{SC} = 59.434 \text{ nC}$, as shown in **Figure S16(b) and (c)**. Integrating a large number of these devices can enable large-scale collection of ocean wave energy to power various devices.

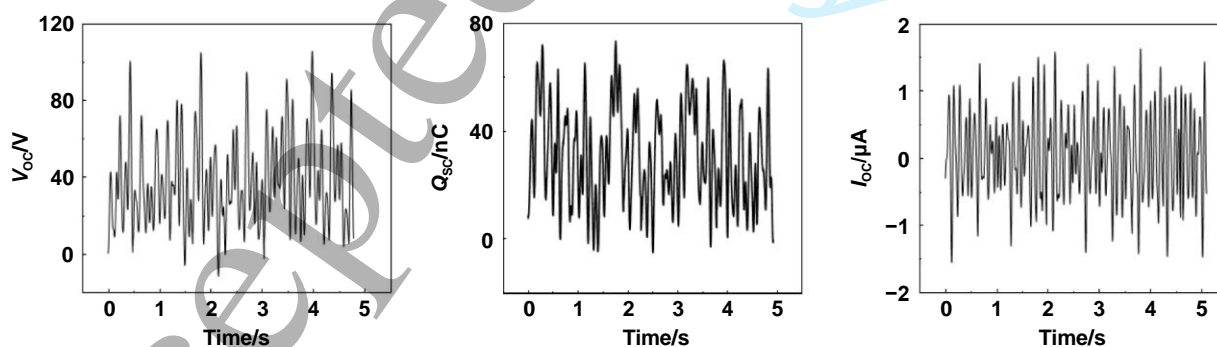


Figure S17. The representation diagram of real irregular wave simulation.

In **Figure S17**, through this study, we were able to observe the performance of yachts in real water environments and concluded that yachts can exhibit excellent performance even under complex irregular water conditions. This result demonstrates the potential application of yacht design in practical situation.

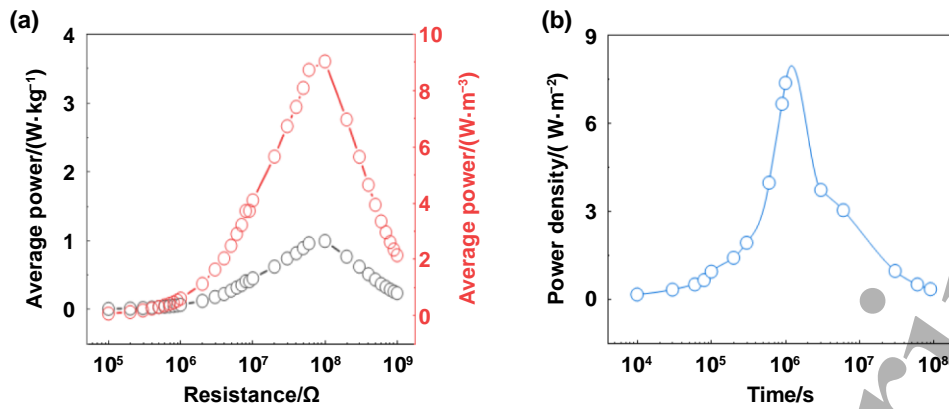


Figure S18. Power density evaluation for the inner and external LS-TENGs. (a) The mass power density and volume power density of internal LS-TENG are dependent on resistance. (b) Area power density and resistance dependence of external LS-TENG.

Figure S18(a) presents the gravimetric and volumetric power densities of the LS-TENG integrated within the windmill as a function of load resistance; the maximum gravimetric and volumetric power densities are $9.0205 \text{ W} \cdot \text{Kg}^{-1}$ and $0.9935 \text{ W} \cdot \text{m}^{-3}$, respectively, when the resistance is $10^8 \Omega$. **Figure S18(b)** shows the areal power density of a single droplet-based external LS-TENG as a function of load resistance; the maximum areal power density is $7.352 \text{ W} \cdot \text{m}^{-2}$ when the resistance is $10^6 \Omega$.

Inter TENG:

$$m = 2.4978 \text{ g}$$

$$m_{total} = 74.934 \text{ g}$$

$$V = \pi r^2 h \times 30$$

$$= 0.68 \text{ m}^3$$

$$P = \int_0^T U^2 / R \, dT$$

$$P = 0.67 \text{ mW}$$

$$p1 = P/V$$

$$= 0.9935 \text{ w/m}^3$$

$$p2 = P/m$$

$$= 9.0205 \text{ w/Kg}$$

External TENG:

$$P = \int_0^T U^2 / R \, dT$$

$$= 4.4116 \text{ mW}$$

$$S = 2.1915 \text{ m}^2$$

$$p1 = P/S$$

$$= 9.0205 \text{ W/m}^2$$

Specifically, we define P as the maximum power in the time period from 0 to T , $p1$ stands for the volumetric power density and V represents the volume of the entire TENG, while $p2$ denotes the mass power density and m is the mass of the entire TENG. $p1$ is the surface power density of the external TENG.

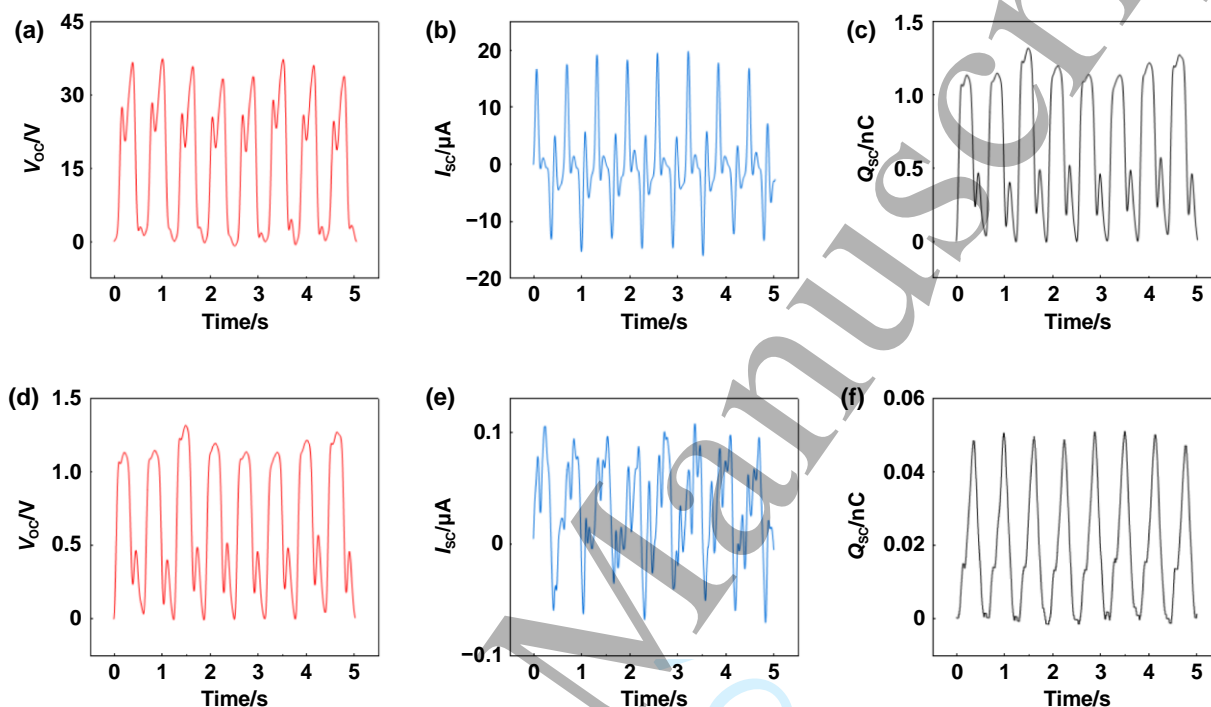


Figure S19. The internal friction material is the electrical output performance diagram of water or oil with 30% salt content. (a)-(c) Electrical output performance diagram of water with 30% salt content. (d)-(f) Electrical output performance diagram of oil.

Due to the phenomenon of solidification of water at subzero temperatures, we characterized the output performance of water with a salt concentration of 30% (with a freezing point of -21 degrees Celsius) and oil. By comparing the results, we found that saltwater exhibited better output performance. It can be used as a substitute for deionized water when applied in extreme environments.